SLAC-PUB-644
August, 1969

Revised Nov. 69.

NEUTRAL BOSON PHOTOPRODUCTION ON HYDROGEN AT HIGH ENERGIES*

BY

R. Anderson, D. Gustavson, J. Johnson, D. Ritson and B. H. Wiik
Stanford Linear Accelerator Center
Stanford University, Stanford, California

W. G. Jones† and D. Kreinick
California Institute of Technology
Pasadena, California

F. Murphy
University of California
Santa Barbara, California

and

R. Weinstein
Northeastern University
Boston, Massachusetts

---

*Work supported by the U.S. Atomic Energy Commission.

† On leave of absence from Imperial College, London, England.

(Submitted to Phys. Rev.)

ABSTRACT

Photoproduction cross sections for neutral pi, eta, rho and phi mesons have been measured at the Stanford Linear Accelerator Center for photon energies between 5 and 17.8 GeV, and t (four-momentum transfer squared) between -.12 and -1.4 $(GeV/c)^2$ using a missing mass technique.

The pion production at lower energies is characterized by a fast fall off with increasing |t| at small |t| values, with a "dip" at $t = -.5$ $(GeV/c)^2$ followed by a secondary maximum around $t = -.9$ $(GeV/c)^2$ and a smooth fall off at larger |t| values. As the incident photon energy increases the dip becomes less pronounced, in contradiction to the expectations of simple Regge theories based only on the exchange of the omega and B trajectories.

Eta photoproduction was measured around 6 GeV and at 9 GeV. The cross section decreases smoothly with t and shows no dip at $t = -.5$ $(GeV/c)^2$, in disagreement with predictions based on Reggeized rho exchange.

Rho production rates agree well with predictions assuming diffraction production. The differential cross section varies approximately as exp(8.5t). The total cross section decreases from 16.0 μbarn at 5.5 GeV to 12.3 μbarn at 17.8 GeV incident photon energy. A quark model relation between π-p elastic scattering and rho photoproduction gives a good representation of the data.

Phi production also appears consistent with the predictions of the diffraction dissociation model.

We also searched for evidence of photoproduction of other particles with mass up to 2 GeV. Production of one particle of mass (1240 ± 20) MeV and width around 100 MeV was observed. No particles with mass between 1300 and 2000 MeV were found. Any particle with cross section larger than 4% of the rho cross section would have been visible.

I. INTRODUCTION

In this experiment we have extended previous data on neutral meson photoproduction cross sections to higher energies and a broader range of four momentum transfers. The experiment was carried out at the Stanford Linear Accelerator Center (S.L.A.C.) using the S.L.A.C. 1.6 GeV/c spectrometer as a missing mass spectrometer. Some preliminary results of this experiment have already been published(1).

Earlier measurements have been made on forward neutral pion photoproduction by groups at D.E.S.Y.(2) and at C.E.A.(3) in the photon energy range from 2 GeV to 5.8 GeV. Their results showed a pronounced dip in the cross sections at a value of the four-momentum transfer squared $t = -.5\ (GeV/c)^2$. There has been considerable speculation on what the form of the energy dependence for this process would be at higher energies(4)(5). The earlier data could be understood within the framework of a conventional Regge theory by assuming omega and B exchange(5). This theory predicted that the B meson exchange would become less important at higher energies and that the process would eventually be completely dominated by omega exchange. Assuming that the rho and omega trajectories were similar, it was then expected that the

neutral pion photoproduction cross section would be similar to the $\pi^- + P \rightarrow \pi^o + N$ charge-exchange cross section, where only rho exchange is permitted, i.e., that the cross section for neutral pion photoproduction would show both a shrinking of the forward peak with increasing energy and a sharp dip at $t = -.5$ $(GeV/c)^2$. Our data extend to photon energies of 15 GeV and appear to be in disagreement with these predictions.

We have also measured eta photoproduction around 6 GeV and at 9 GeV. Lower energy data(6) covering a similar range in t exist from experiments at the C.E.A. The results are mainly interesting for their behavior near $t = -.5$ $(GeV/c)^2$. In conventional Regge theory the process is expected to have a large contribution from rho meson exchange and therefore it should show a sharp dip at $t = -.5$ $(GeV/c)^2$. No such dip is observed.

Our measurements of neutral rho photoproduction extend to higher energies than previous data(7)(8)(9)(10). The results of these experiments at lower energies have been successfully explained in the framework of the vector meson dominance theory. According to this theory the cross section for photoproduction of a vector meson V^o should be proportional at high energies to the cross section for the elastic scattering of transversely polarized vector mesons from hydrogen, i.e.

$$\frac{d\sigma}{dt}(\gamma + p \rightarrow V^o + p) = \frac{\alpha}{4}\left(\frac{4\pi}{\gamma_V^2}\right)\frac{d\sigma}{dt}(V^o_{tr} + p \rightarrow V^o_{tr} + p), \qquad (1.1)$$

where $\alpha = 1/137$ and γ_V describes the coupling of a virtual vector meson to a real photon. On the basis of a broken SU(3) quark model(11), the cross section for the elastic-scattering process $\rho^o + P \rightarrow \rho^o + P$ is given by:

$$\frac{d\sigma}{dt}(\rho^o p) = \left(\frac{1}{2}\sqrt{\frac{d\sigma}{dt}(\pi^+ p)} + \frac{1}{2}\sqrt{\frac{d\sigma}{dt}(\pi^- p)}\right)^2 \qquad (1.2)$$

These relations are well satisfied for neutral rho photoproduction over the whole kinematic range covered in this experiment.

Previous to this experiment little experimental data was available on the photoproduction of the phi meson(8)(12). Phi production, though small, should be largely diffractive. The results of this experiment in the energy range between 6 and 18 GeV support this assertion. The t dependence of the cross section is again reproduced with a broken SU(3) quark model prediction (11)(13).

No previous firm observations(14) have been made on the photoproduction of higher mass mesons at high energies. We observed the production of a meson in the mass region around 1240 MeV, tentatively identified with the B meson. We searched for vector meson production in the region of masses 1.3 GeV to 2 GeV, and might have expected to observe the $J^{PC} = 1^{--}$ "daughter" to the rho meson around 1500 MeV. No such meson was found.

II. EXPERIMENT AND APPARATUS

A. Experimental Arrangement

The experiment was carried out at the Stanford Linear

Accelerator Center. The layout of the experiment is shown in Fig. 1. The momentum analyzed electron beam was focussed onto an aluminum radiator, .03 radiation lengths thick, located about 150 ft. upstream of the target. A sweeping magnet, placed just after the radiator, deflected the main electron beam into a beam dump. The photon beam was then collimated to the required size by a high power water cooled collimator (C-10) before impinging on the liquid hydrogen target. Secondary collimators were set up to intercept any halo of the beam remaining after the collimation by C-10. There were also several sweep magnets in the beam line to remove electron spray produced by these collimators. The photon beam finally stopped in a Secondary Emission Quantameter (S.E.Q.) located approximately 100 ft. downstream from the target. This S.E.Q. was our primary beam monitor. In addition the beam intensity was monitored by a Cerenkov monitor as well as a Secondary Emission Monitor (S.E.M.), both located in the front of the target as indicated in Fig. 1. The intensity of the photon beam incident on the target was typically 5×10^{11} equivalent quanta per second.

The target used was of a condensation type(15). The target cell was a cylinder, 15 in. long and 2 in. in diameter, made out of .008 in. thick mylar with thin aluminum end caps. A "dummy cell" and a "no cell" position were also available.

B. Spectrometer and Counter System

The S.L.A.C. 1.6 GeV/c spectrometer(16) was used to analyze the recoiling protons. It is a weak focusing ($n = 0$), second-order corrected, 90° vertical bend magnet with a radius of

100 in. The momentum acceptance and the acceptance in production angle are defined by the size of the counters in the focal plane. The azimuthal angle ($\Delta\varphi$) and the useful target length were determined by remotely moveable slit systems placed at the spectrometer entrance. For this experiment the total acceptance was $\frac{\Delta p}{p} \Delta \Omega = 6.8 \times 10^{-5}$ sterad. and the useful target length was typically about 7 in.

The spectrometer focussed production angles and momenta onto a single focal plane which was normal to the direction of the focussed particles and had a linear dispersion of 1.66 in. per percent in momentum and .32 in. per mrad in angle. The resolution was ±.08% in momentum and ±.4 mrad in angle. The locus of particles from a particular two body reaction can be approximated by a straight line over the small momentum and angle acceptance of the spectrometer focal plane. Hence a two body process can be selectively detected by a hodoscope counter aligned along the appropriate kinematic curve. This technique eliminated complex decoding and made it possible to record several events during the 1.6 μsec long S.L.A.C. beam pulses with simple electronics.

The momentum calibration and the solid angle had been previously determined both by a wirefloat measurement and by running a well defined electron beam from the accelerator directly into the spectrometer. The estimated error was ±.2% in the momentum calibration and ±3% in the total acceptance $\frac{\Delta p}{p} \Delta \Omega$. We estimate that the uncertainty in the determination of the production angle with respect to the direction of the photon beam was ±0.3 mrad.

The spectrometer and the counter system are shown in Fig. 2; the counter system is shown in more detail in the insert. The telescope consists of five scintillation counters (S9 - S13) made out of Pilot B plastic; S9 and S10 were 7 X 11 X .5 in., and S11, S12 and S13 were 10 X 14 X .5 in. Between S10 and S11 and between S11 and S12 there were remotely variable absorber changers. A missing mass hodoscope consisting of 8 elements, each .75 X 10 X .25 in., was located between S9 and S10. For counters S9 and S10 Amperex XP1020 photomultiplier tubes were used; for all other scintillation counters RCA 7850's were used. A threshold Lucite Cerenkov counter (9 X 13 X 2 in.) was inserted between S10 and S11. The counter was so constructed that only light which was internally reflected could reach the phototubes. The outputs of the four RCA 8575 photomultiplier tubes used to view the Lucite were added linearly. The counter was 98% efficient for pions and counted protons with less than 2% efficiency below 1000 MeV/c increasing to 6% at 1400 MeV/c. The whole counter system was remotely rotatable so that the hodoscope counters could be aligned along lines of constant missing mass in the focal plane.

For low t values ($|t| < .4$ $(GeV/c)^2$), the protons were identified by range and pulse height using the first few trigger counters. At higher $|t|$ values the threshold Cerenkov counter was used in veto to provide additional rejection against pions. The ratio of the pion flux to the proton flux incident on the counters was typically 1:1 near the π^o threshold and the above criteria reduced the pion contamination to the 1% level. The last two scintillation counters S12 and S13 had their biases set low and

were put in coincidence with the threshold Cerenkov counter to monitor the flux of produced π^+ mesons.

To measure the efficiencies of the system for protons and pions we used the chopped S.L.A.C. electron beam and a time-of-flight system(17). This provided us with a clean separation of protons and pions and allowed the detection efficiencies of the system to be determined. The efficiencies of the individual hodoscope elements were determined for each run and were near 100%.

C. Electronics

Fig. 3 shows a simplified block diagram of the electronics. Standard 100 Mc modules(18) were used for the logic. The event rate was quite high, up to 6 counts in the 1.6 μsec long beam pulse. The interesting rates were therefore all fed into fast 100 Mc scalers(19) and stored there for the duration of an experimental run. After each run the scalers and other relevant data were read by the S.L.A.C. SDS-9300 computer.

D. Beam Monitors

The primary beam monitor was a non-saturating quantameter(20). The quantameter was fully evacuated and consisted of twenty copper plates 0.5 in. thick alternated with nineteen foils of gold plated aluminum each 0.0005 in. thick. The device was calibrated against the S.L.A.C. silver calorimeter(21) as well as against a Faraday cup. The average calibration constant was 2.92 electrons/GeV for a voltage of +750 volt. The absolute calibrations were repeated periodically during the course of the experiment and were found reproducible within one percent.

However we assigned an overall error of ±2% to our absolute calibration value.

The relative stability of our monitor systems, when conditions were carefully standardized, was ±.2%. We used the S.L.A.C. photon beam Cerenkov monitor(21) for an additional check. This consisted of a tube 30 in. long filled with He gas at about 1 atm. The light was focussed onto a photomultiplier tube, whose output was then integrated. The ratio of the Cerenkov monitor to the S.E.Q. remained constant to fractions of a percent for periods of hours.

E. Data Accumulation and Reduction

The choice of the hodoscope angle determined the angular production width $\Delta\theta$ accepted by one hodoscope counter and the range of angles was then divided into bins, each $\Delta\theta$ wide. This bin width was typically about 2.8 mrad. To reduce our sensitivity to small drifts in the apparatus, the data were accumulated in an interlaced pattern over the angular range of interest and each angular point or bin was measured on several and in many cases on all 8 hodoscope counters. Since the π^+ meson yield curve, measured simultaneously by a coincidence between counters S12, S13, and the threshold Cerenkov counter, should vary smoothly with angle in this kinematic region, a valuable additional cross-check on the beam and monitor stability was available.

Each run at a given angle lasted typically 5 minutes. After the run the relevant data were all read in, stored and recorded on magnetic tape by the S.L.A.C. SDS-9300 computer. The hodoscope data were accumulated in bins and an automatic plotting

machine plotted each run individually to aid the experimenter in checking for consistency. The accumulated data could be plotted on demand and selected runs on the data tape could be added to or removed from the accumulation at any time.

Frequently the counting rate was measured as a function of beam intensity. This rate check was done by remotely varying the size of the photon collimator, leaving the beam structure as well as the beam steering intact.

Occasionally empty target runs were made. The empty target rates were negligibly small compared with the full target rates.

Subsequent to this the following steps were taken:

1. Some runs were edited or discarded because of procedural errors in data-taking.

2. Each run was corrected for dead time losses and accidental coincidences using the measured rate dependence. This combined correction was always kept less than 5%.

3. Most data points were repeated on several elements of the hodoscope array. Differences in counting efficiency among the hodoscope elements were accounted for before these data points were combined to obtain our final yield curves. Because of the large degree of internal repetition and redundancy the data could be cross-checked for internal consistency, relative monitor drifts, etc.(22). In the vast majority of runs the external and internal error assignments were in agreement. In a few cases a small monitor change was detected and was found to correlate with a small change in the independently detected π^+ meson rate. These

few runs were corrected or eliminated.

4. We combined all the corrected data at fixed |t| values and end-point energies into yield curves as a function of the spectrometer angle.

F. Analysis of the Yield Curves

The production of a resonance particle X^o in the reaction $\gamma + P \rightarrow X^o + P$ corresponds to a "step" in the detected recoil proton yield measured as a function of angle for a fixed photon end-point energy. This missing mass technique is very powerful for avoiding the complexities of detecting rapidly decaying particles as well as for surveying for the production of all possible particles in the same experimental set up. To see how each produced resonance must correspond to a "step" in a yield curve, let us first consider a monochromatic photon beam with energy k. In this case the missing mass is uniquely given by:

$$M_X^2 = 2k(p \cdot \cos\theta - T) - 2MT \qquad (2.1)$$

Here p and θ are the momentum and angle, M the mass and T the kinetic energy of the recoiling protons. Hence, by measuring the 3-momentum of the recoiling proton the mass of the produced "particle" X^o is determined. Fig. 4 shows the laboratory momentum of the recoil protons plotted versus angle in the laboratory for a fixed photon energy of 11.5 GeV. It is clear from this figure that by varying the spectrometer angle and keeping the momentum fixed we get separate peaks corresponding to the different mass particles. In reality we are dealing with a bremsstrahlung beam,

but for a fixed end-point energy k_o of the photon spectrum and a fixed recoil momentum of the proton we can always define a limiting angle θ_o such that $M_X^2 = 0$. This corresponds to Compton scattering on the proton. At larger angles there are no kinematically allowed protons. At all smaller angles protons from the Compton process are kinematically allowed. As we now move towards smaller angles with the spectrometer each new resonance will show up as a "step" on a rising yield curve.

Fig. 5A shows such an experimentally measured yield curve for k = 11.5 GeV and t = -.7 $(GeV/c)^2$, and the breakdown of the yield into counts from the production of pions, rhos, phis and nonresonant background. There was an appreciable yield of protons beyond the allowed kinematic limit because of the rescattering of forward produced particles. This background was associated with the full target and was very small from the dummy target. As can be seen from Fig. 5A, π^o production showed up as a step on this "ghost proton" background. The angular resolution was not sufficient to separate the protons associated with π^o production from those associated with Compton scattering, but at this particular angle and energy the Compton effect should be negligibly small compared with π^o production. The shape of the leading edge of the pion step was almost completely determined by the angle changes due to multiple scattering of the recoil protons as they traversed the target. As the angle was decreased, recoil protons from successively higher masses were observed and the steps due to rho and phi mesons can be clearly seen. A threshold missing mass scale is provided for convenience, although in

reality photoproduction of all lower missing masses can produce recoil protons at the same angle and momentum. For example, at the angle in Fig. 5 corresponding to phi's made by 11.5 GeV photons, neutral rho's are produced by 8.3 GeV photons, and neutral pions are produced by 4.8 GeV photons.

As a check on our procedures, yield curves were occasionally taken at closely adjacent energies E_1 and E_2. By subtracting the two yields with the appropriate corrections, a curve was obtained which corresponded to photoproduction by photons in the range E_1 to E_2. These subtracted curves showed the structure to be expected from a nearly "monochromatic" photon beam. Fig. 5B shows such a curve obtained by subtracting the yields obtained with photon end-point energies of 13 GeV and 11.5 GeV. Almost identical curves can be obtained by "differentiating" or taking successive differences of the yields on an integral yield curve obtained at one end-point energy. Fig. 5C shows such a curve obtained by taking successive differences on the integral curve shown in Fig. 5A. Note that the subtracted yield curve Fig. 5B and the first difference curve Fig. 5C appear almost identical.

Cross sections were extracted by making a least-squares fit to a full sweep, fitting the positions and shapes of the various particles' yields and assuming smooth backgrounds due to ghost protons and multi-particle production. The computer program accounted for kinematic factors, the correct bremsstrahlung spectra, resolution, and the variation of the cross section with energy. Subtracted yield curves, where available, were

similarly fitted. The π^o, η, and φ steps were fitted also by eye, since the computer fits described above, although having the advantage of objectivity, suffer from inflexibility and the tendency of the large ρ^o yield to dominate the solutions. The two approaches were considered to be complementary, and disagreements usually reflected genuine ambiguities in interpretation. These ambiguities were accounted for in our quoted errors. A detailed discussion of the analysis is available in Ref. 22.

Our final cross sections include monitor calibrations, spectrometer calibrations, counter efficiencies, etc. Table I lists the various corrections, their magnitudes and our estimates of the typical uncertainties in these corrections.

III. π^o CROSS-SECTIONS

Fig. 6A shows a typical integral yield curve plotted against missing mass squared in the π^o mass region. The sharp step due to the onset of the π^o production is clearly seen. In the same figure the differential yield curve as derived from the integral curve is also shown. In this representation π^o production appears as a peak. The kinematic threshold for two pion production is close to that for single pion production. However since two pion production is a three body process it does not lead to a sharp step but to a smoothly rising yield curve starting at the threshold. This process was accounted for in the fitting programs by a polynomial starting at the two pion threshold and including the experimental resolution. The difference between a three body and a two body process is sufficiently marked that we believe that this process is well

accounted for in our cross section determination and in our error assignments.

Since the experimental resolution is not sufficient to separate π^o production from Compton scattering, the cross sections extracted from the experimentally determined step heights must be reduced by the contribution of the Compton scattering. For this correction we assume the Compton cross section to be of the form $d\sigma/dt = A\, e^{Bt}$ where $B = 8.5$ (GeV/c)^2, e.g. the same slope as observed in the ρ^o photoproduction on the proton. $A = .68$ μb/(GeV/c)^2 was determined from the total γ-p cross section using the optical theorem. The total γ-p cross section was set equal to 115 μbarn at high energies, in accordance with recent measurements(23). The correction is important (50%) at low $|t|$ values and high energies. We estimate the correction to be known to ±20%.

In Fig. 7, $d\sigma/dt$ determined from the step heights is plotted versus t for primary photon energies of 6, 9, 12, and 15 GeV. The data are characterized by a fast drop of the cross section at low $|t|$ values, a dip close to $t = -.5$ (GeV/c)^2 followed by a secondary maximum at $t = -.9$ (GeV/c)^2, and a smooth fall off with increasing $|t|$-values. With increasing photon energies the dip gradually becomes less pronounced.

Fig. 8 shows our data at 6 GeV together with the D.E.S.Y. results(2) at 5 GeV and 5.8 GeV for comparison. Plotted is $s^2\, d\sigma/dt$ versus t. The agreement is very satisfactory.

In Fig. 9 $d\sigma/dt$ versus $(s-m^2)$ is plotted for constant values of t. The D.E.S.Y.(2) data at lower energies are included

in these plots. A least squares fit to the data of the form $d\sigma/dt \sim (s-m^2)^{2\alpha-2}$ was made to the data at 3 GeV and above and is shown as the solid lines in Fig. 9. It clearly gives a very reasonable simultaneous representation of both our data and the D.E.S.Y. data. There is a small but significant amount of shrinkage with the effective Regge α decreasing from $\alpha = .16 \pm .05$ at $t = -.7$ $(GeV/c)^2$ to $\alpha = -.2 \pm .05$ at $t = -1.4$ $(GeV/c)^2$. Below $|t| = .5$ $(GeV/c)^2$, α remains close to 0. However these points are more uncertain, since for low $|t|$ values and high energies the spread of photon energies corresponding to the width of the π^o step becomes large. This spread arises from the angular uncertainty due to the multiple scattering of the recoil protons at small $|t|$ values combined with the kinematic factor $(dk/d\theta)_{p=const.}$ which increases rapidly with decreasing $|t|$. The quoted errors on the low t points at high energies are largely systematic in origin and arise from our estimates of the above uncertainties. At high $|t|$ values the resolution becomes entirely adequate and the quoted errors are mainly statistical.

The π^o photoproduction at forward angles and high energies was originally expected(5) to be dominated by Reggeized particle exchange in the t-channel. Charge conjugation invariance requires the exchanged t-channel particle to be odd under C. Hence, of the established particles only the neutral rho, omega, phi and B (or its isoscalar "relative" in the $J^P = 1^+$ octet) need be considered. From a comparison of the coupling constants one would expect omega exchange to dominate everywhere except in the vicinity of $t = -.5$ $(GeV/c)^2$, where the omega trajectory goes

through zero. This |t| value corresponds to a supposed nonsense zero in the amplitude arising from omega exchange with a resulting dip in the cross section. Since the omega trajectory is very close to the rho trajectory and phi exchange should be negligible, it was expected that in this dip region around -.5 $(GeV/c)^2$ the cross section would be dominated by B exchange. At lower energies this picture agreed well with the differential cross section measurements at D.E.S.Y. and C.E.A.(2)(3). This model further predicted that the dip in π^o photoproduction would become more pronounced at higher energies and that the energy dependence of $d\sigma/dt$ would display strong shrinkage.

Neither of these predictions appear born out by the results of this experiment. As we go to higher energies the dip seems if anything to disappear and the shrinkage is much less than expected(5). For instance at $t = -.9\ (GeV/c)^2$, $d\sigma/dt \sim (s-m^2)^{-1.8}$ whereas from the accepted omega trajectory(24) we would expect $d\sigma/dt \sim (s-m^2)^{-3}$. That the cross section in the dip region is not dominated by B exchange (or the exchange of the isoscalar member of the "B octet") is also shown by measurements with polarized photons at 3 GeV(25). These polarized photon measurements have shown that the dominant exchange at these energies in the region of the dip has natural parity, thus excluding B exchange.

The combined experimental data on π^o production therefore can not be described in terms of simple Regge exchange. However by including cuts or absorption in addition to the elementary Regge exchange reasonably successful fits to the π^o photoproduction data have been achieved(26)(27)(28)(29). The

simplest cut term is the one that corresponds to the exchange of the pomeron P together with the omega. The effective trajectory (t) can in this case be written as:

$$\alpha_C(t) = \alpha_\omega(0) + \alpha_p(0) - 1 + \frac{\alpha'_\omega \alpha'_p}{\alpha'_\omega + \alpha'_\omega} t \qquad (3.1)$$

Since this trajectory for physical |t| values lies higher than the omega trajectory we would expect the cut to dominate the cross section at sufficiently high energies.

Capella and Tran Thanh Van(26) attempt to fit the differential cross section as well as the polarized photon data assuming only omega and omega-pomeron exchange. They achieve a good fit to the data using 5 free parameters. Contogouris and Lebrun(27) investigate the relationship between the pole terms and the cut terms, and compute the cut terms corresponding to omega exchange from a model. They achieve good fits to forward π^o photoproduction as well as forward π^+ photoproduction using the same set of parameters.

Fröyland(28) introduces the rho and rho-pomeron cut in addition to the omega and omega-pomeron cut. He also achieves a good fit to the data, but this involves a large number of free parameters which are not uniquely determined from the experiment.

Blackmon, Kramer and Schilling(29) try to fit the data with omega and rho exchange including absorption. They conclude they cannot get a good fit to the data with this model. They achieve a reasonable fit to all π^o data by including B exchange in addition. However the B meson trajectory, $\alpha(t) = .4 + .4t$ as

determined from the fit, is much higher than expected and the slope is rather small.

It has been conjectured that a fixed pole at J = 0 could be present in the π^o photoproduction(30). Such a pole would lead to a s^{-2} dependence of the cross section for sufficiently high energies in the region where α is negative. The present data seems to give no evidence for this.

Dar, Weisskopf, Levinson and Lipkin(31) have compared the vector dominance prediction of π^o photoproduction with the experimental data. Unfortunately the strong interaction cross sections are not known at high energies and the low energy measurements are not very accurate. Within the errors of the experiments the V.D.M. prediction is well fulfilled at 6 GeV using $(\gamma_\rho^2/4\pi) = .5$.

IV. ETA PRODUCTION

Fig. 10A shows an integral yield curve in the region of the eta mass, at a primary photon energy of 5.5 GeV and $t = -.5\ (GeV/c)^2$. The corresponding differential yield curve is shown in Fig. 10B. In both representations the eta production is clearly seen.

Measurements of the eta yield are rendered difficult by the proximity to the rho meson yields. At low energies and moderate |t| values the separation from the rho signal is clear. At 9 GeV it is still possible to distinguish eta yields in the region of $t = -.7\ (GeV/c)^2$. At higher energies the separation of the eta step from the rising rho yield was ambiguous and we do not include these measurements.

Fig. 11 shows the measured eta cross section $s^2\ d\sigma/dt$ as a function of t for primary photon energies of 5.5, 6.0, 6.5 and 9 GeV. For comparison the measured π^o cross section curve at 6 GeV is shown as the dotted line. The difference between the eta and pi angular distributions is very striking. Whereas the pi cross section shows a dip around $t = -.5\ (GeV/c)^2$ followed by a secondary maximum, the t dependence of the eta cross section for t between $-.3\ (GeV/c)^2$ and $-1.1\ (GeV/c)^2$ shows no structure. For the range of energies covered in this experiment the energy dependence of the cross section is consistent with s^{-2}.

Fig. 12 shows a comparison of our data (assuming s^{-2}) with the C.E.A. data(6) taken at a primary photon energy of 4 GeV. Plotted is $s^2\ d\sigma/dt$ versus t. The agreement is moderate, our results appearing somewhat systematically higher than the C.E.A. results. This might arise either from an energy dependence other than s^{-2} or from experimental biases. The integral yield method we used is less likely to result in experimental bias than the C.E.A. coincident photon measurements which involved a variety of cuts on the data to extract the cross sections.

The photoproduction of eta's at forward angles should have a large contribution from Reggeized rho exchange. This would then lead to a dip in the cross section in the vicinity of $t = -.5\ (GeV/c)^2$ where the rho trajectory passes through 0. The absence of such a dip in the data is puzzling. The class of theories(32) which explain the dip in π^o photoproduction and π^-p charge exchange as due to interference terms between the pole terms and the cut terms could lead to a natural explanation of

both the neutral pi and eta photoproduction results.

By assuming only rho exchange Dar and Weisskopf(33) relate the eta cross section to the reaction $\gamma + P \rightarrow \omega + N$. Using the data taken at 3.25 (GeV/c) they achieved reasonable agreement with this experiment using $\gamma_\omega^2/4\pi = 2.9$. B. Gorczyca and M. Hayashi(34) include omega and B-exchange as well. They also achieve reasonable agreement with the data. Both predictions are plotted in Fig. 12.

These models(33)(34), although giving reasonable predictions, do not clarify the basic underlying mechanisms involved in eta production.

V. RHO-OMEGA PRODUCTION

In the course of this experiment we obtained about 60 yield curves suitable for extracting ρ^o cross sections

Fig. 13A shows a typical yield curve. Fig. 13B is a plot of the first differences of the yields, and has the distinctive rho peak at around 765 MeV. Fig. 13C shows a difference curve obtained by subtraction between two close end-point energies. All three curves contain essentially the same information. We had insufficient resolution to distinguish omega production clearly from neutral rho production. For the purposes of analyzing the data we assumed that the omega cross sections were 10% of the rho cross sections. This should be a good approximation since at high energies the non-diffractive part of the omega production is small and the ratio between omega and rho should be given by SU(3). This has been confirmed experimentally(12).

It was hard to draw definitive conclusions as to the

shape of the rho decay spectrum. At high energies and low t values the resolution of the apparatus became comparable to the width of the rho. At low energies, although the resolution was very adequate, the background of multipion events under the rho peak became large and produced some ambiguities in the interpretation. These ambiguities were most serious with respect to the shape and less serious with respect to the total cross section.

A large number of shapes and widths for the rho-meson were investigated and are listed below:

a. A relativistically correct generalization of the simple Breit-Wigner form, as described by Jackson and Selleri(35).

b. A form suggested by Ross and Stodolsky(36) where the above shape is multiplied by the additional factor of $(m_\rho/m)^4$. Although this factor is disputed, at least one experiment indicates it may be a good description of the rho shape(8). Other powers of (m_ρ/m) were also tried.

c. The Söding interference model(37). Because our method integrates over the whole resonance the interference term tends to cancel out, and the results are not significantly different from those for the Jackson shape.

d. A simple nonrelativistic Breit-Wigner shape.

The background from nonresonant multipion production was estimated with a polynomial, which was kept to as few terms as possible consistent with a reasonable fit. With different assumed rho shapes, the fitting program divided the observed yield into background and rho signal differently. In general, cross sections

obtained with the different models disagreed by five to ten per cent, with the Jackson shape giving values about seven per cent systematically higher than the Ross-Stodolsky. Our data did not significantly prefer any one shape. The Jackson shape tended to give better fits at high energies and high t values. The Ross-Stodolsky shape gave better fits at low t values and low energies, and gave poor fits at high energies and high t values.

Various experiments have measured rho widths anywhere between 90 and 160 MeV, and masses between 720 and 780 MeV (7)(8)(9)(10). Both these parameters were at first treated in this experiment as unknowns to be determined at each energy and momentum transfer. There was no observable dependence of the rho mass on s or t. The best fit mass value depended, of course, on the shape used. The Jackson form led to a mass of (765 ± 20) MeV in agreement with the results of McClellan et al.(9). The Ross-Stodolsky form gave a value 10 MeV to 20 MeV higher. The large rho mass shift sometimes reported to be observed in photoproduction experiments(7)(8)(10) was not observed in this experiment. For each yield curve a best rho width was determined by stepping the input rho width in 15 MeV increments between 80 and 170 MeV, simultaneously adjusting the background polynomial to give a best fit to the data. The error was taken to correspond to the point where the chi-squared probability had fallen to half of its best value. This criterion gave typical errors of ±30 MeV. This large error arose because changes in the background polynomial could accommodate changes in the trial rho width. In general the preferred width was relatively independent of the rho

shape chosen. As with the mass there was no systematic dependence of width on s or t. Including possible systematics a best width of (127 ± 25) MeV was obtained.

All subsequent cross section fitting, at all energies and momentum transfers, was made with the Jackson shape(a) for the rho with a width of 125 MeV and a mass of 765 MeV plus a 10% omega contribution. The variations of the derived rho cross sections with assumed rho widths was, on the average, five per cent for a 10 MeV change in width. For each yield curve the sensitivity of cross section to width and the uncertainty in the width were used to estimate errors. In general the presence of non-resonant background was the cause of the above systematic uncertainties and the assigned systematic error was approximately equal to ±30% of the nonresonant background. The nonresonant background was largest at low energies where processes other than diffractive are still important, and at high t values where again the diffractive contributions are not so dominant.

Our results, when analyzed consistently, showed high internal consistency. This internal consistency does not necessarily correlate with real precision in the cross section determinations, and our quoted results may therefore be systematically distorted to run either high or low through our error bars.

Fig. 14 shows a comparison of our data in the energy range 5.5 GeV to 6.5 GeV with a fit to the D.E.S.Y. data(38) at nearby energies. Also included on the figure are the results of McClellan et al.(9) at 6 GeV. The agreement between the three sets

of data is good.

Both from the vector dominance model and on more general grounds(39) we should expect for |t| values where diffractive scattering is dominant that the photoproduction of ρ^o mesons will be related by a constant of proportionality C_ρ to elastic ρ^o-p scattering:

$$\frac{d\sigma}{dt}(\gamma\rho^o) = C_\rho \frac{d\sigma(\rho^o p)}{dt} \qquad (5.1)$$

Substituting the quark model prediction(11) from Eq. 1.2 into this relation, we obtain:

$$\frac{d\sigma}{dt}(\gamma\rho^o) = C_\rho\left(\frac{1}{2}\sqrt{\frac{d\sigma}{dt}(\pi^+ p)} + \frac{1}{2}\sqrt{\frac{d\sigma}{dt}(\pi^- p)}\right)^2 \qquad (5.2)$$

Fig. 15 shows a comparison between our results and these theoretical predictions using the elastic pion scattering data of Foley et al.(40) with C_ρ as our only adjustable parameter. The theoretical prediction is plotted as the solid lines together with the experimental data points. The agreement is remarkably good over the t-range from -.2 $(GeV/c)^2$ to -.7 $(GeV/c)^2$ at 6.5 GeV and over the entire t-range at higher energies.

It does not seem possible that this agreement with theory is fortuitous, and we therefore believe the error is small in extrapolating our data to t = 0 using the above predicted shape, at least at the higher energies. Table II gives values of $(d\sigma/dt)_{t=0}$ and of σ_T obtained from this shape with a single best value of C_ρ. We also give values of $(d\sigma/dt)_{t=0}$ and σ_T where we

assume the shape is represented by the above formula over the |t| value range of .1 $(GeV/c)^2$ to .7 $(GeV/c)^2$ but permit C_ρ to vary with energy. The forward cross section analyzed either way drops from an average value of 130 to 140 $\mu b/(GeV/c)^2$ around 6 GeV to an average value 102 $\mu b/(GeV/c)^2$ around 17 GeV.

McClellan et al.(9) report the cross section at t = 0 as $\sim$ 130 $\mu b/(GeV/c)^2$ in the range of 5 GeV to 10 GeV. Within errors this is consistent with our values. However their values show less of a trend to decrease with energy over this range. We note that their cross section determinations, like ours, are dependent on the specific shape and background assumptions. Their measurements, based on observation of the final two pion state, have less severe background problems than ours. However, our statistical precision is much higher and our integral yield measurements are automatically summed over the rho mass spectrum with nearly the appropriate weights. We are thus less sensitive to exact spectral shapes than are methods based on taking weighted samples in the neighborhood of the rho decay peak.

We can use the vector dominance relation:

$$\left.\frac{d\sigma}{dt}\right|_{t=0} = \frac{\alpha}{4}\left(\frac{4\pi}{\gamma_\rho^2}\right)\frac{\sigma_T(\rho^o p)^2}{16\pi} \qquad (5.3)$$

to relate our mean value of C_ρ to $\gamma_\rho^2/4\pi$, the usual vector dominance factor. The result is $\gamma_\rho^2/4\pi = 0.61$. If instead we use σ_T = 30mb at 9 GeV, from Bulos et al.(41), we obtain $\gamma_\rho^2/4\pi = 0.7$. If we assume σ_T = 39mb at 6 GeV, from McClellan et al.(42), we get $\gamma_\rho^2/4\pi = 1.09$. Thus a value of $\gamma_\rho^2/4\pi = 0.45$ is not consistent with

a vector dominance theory relating the ρ^o-photoproduction cross section at t = 0 of 120 to 130 $\mu b/(GeV/c)^2$, as measured in this and other experiments, to rho-nucleon total cross sections in the range 30 to 40mb(8)(41)(42).

VI. PHI PRODUCTION

The phi meson production cross sections were considerably smaller than the neutral rho cross sections. The proton yield from phi production comes in a region where the lower energy components of the bremsstrahlung beam also produce a very large yield of protons associated with rho production and non-resonant background. As with the rho, the signal to noise ratio improved at high energies where the diffractive processes dominated, and measurements at low |t| values were difficult because of the poor angular resolution caused by the multiple Coulomb scattering in the target. Fig. 16A and 16B show typical integral and first difference yield plots in the region of the phi. While the small decay width of the phi gave a sharp and distinctive threshold in the yield curve, very good statistical precision was necessary to distinguish the phi production from background processes underneath the phi step. We analyzed the phi yield curves assuming relatively smooth backgrounds and made conservative error assignments on the basis of a detailed statistical analysis. A typical yield curve consisted of 20 points, each with a standard deviation of ±.3%, in the mass range 950 to 1150 MeV, and with a phi-step change of 3% superimposed on the background. Under these conditions we typically assigned to the step height an error of

$\sqrt{2}$ times the absolute standard deviation for one yield point, or a relative error on the final quoted phi-cross section of about ±15%.

Fig. 17 shows our results for different energies plotted versus t. We have included for comparison with our 6.5 GeV data the D.E.S.Y. point of Asbury et al. at $t \simeq 0$ and at higher $|t|$ values the results of the D.E.S.Y. bubble chamber experiment(8). Agreement is satisfactory.

The solid line represents the theoretical predictions based on the assumptions of the quark model(40). We assumed(43):

$$\frac{d\sigma}{dt}(\gamma\varphi) = C_\varphi \frac{d\sigma}{dt}(\varphi p) \qquad (6.1)$$

$$\frac{d\sigma}{dt}(\varphi p) = \left(\sqrt{\frac{d\sigma}{dt}(K^+ p)} + \sqrt{\frac{d\sigma}{dt}(K^- p)} - \sqrt{\frac{d\sigma}{dt}(\pi^- p)}\right)^2 \qquad (6.2)$$

The K^+p and K^-p cross sections were taken from the experiment of K. J. Foley et al.(44). The t dependence is well represented by the quark relation. There is an indication in the data of a decrease in C_φ and a corresponding decrease in the total phi cross section with increasing photon energies. The fit to the data with varying C_φ gave, at 6 GeV incident photon energies, a forward cross section of $(3.2 \pm .4)$ μb/(GeV/c)^2 and a total φ-cross section of $(.71 \pm .08)$ μb. Averaged over photon energies between 11.5 GeV and 17.8 GeV, the forward cross section was

$(2.1 \pm .2)\ \mu b/(GeV/c)^2$ and the total cross section was $(.45 \pm .04)\ \mu b$. A change in C_φ with energy is in some disagreement with the quark model. However since the connection equation(6.2) between the theoretical φp elastic cross sections and the physically observed strong interaction cross sections involved large subtractions this apparent discrepancy does not seem too significant.

Our value for $\gamma_\varphi^2/4\pi$ as derived from the average value of C_φ is 9.8. Within the uncertainties in the present values of $\gamma_\varphi^2/4\pi$ this is in reasonable agreement with the theoretical expectations(45) that the ratio $\gamma_\rho^2:\gamma_\varphi^2$ should be 1.33:9.

VII OTHER MESON PRODUCTION

The X^o (958) meson is expected to be produced with cross sections comparable to those of the eta meson(33). However the X^o meson was not clearly resolved from the rho meson. Upper limits to the cross sections in the 6 GeV range gave values less than two or three times the observed eta cross sections, in no contradiction to the theoretical expectation.

At high energies we saw indications for the production of a broad resonance centered at (1240 ± 20) MeV with a width of around 100 MeV. We covered an appropriate range of mass values for measuring the production of a 1240 MeV mass particle on about 15 sweeps. All of the sweeps taken at 13 GeV and 14.5 GeV in the range of $t = -.3\ (GeV/c)^2$ to $t = -.7\ GeV/c)^2$ gave evidence for such a resonance. Fig. 18 shows a representative mass sweep obtained by subtracting the yields taken at 14.5 GeV and 13 GeV for $t = -.5\ (GeV/c)^2$. At higher energies the mass scale was

compressed, and at lower energies the backgrounds increased, making the signals less clear. Qualitatively this meson (or possibly mesons) was produced with cross sections of the same order as the phi in the energy range 13.0 GeV to 14.5 GeV, and the |t| value range of .3 $(GeV/c)^2$ to .7 $(GeV/c)^2$. We tentatively identify this signal with the B meson whose quantum numbers $J^{PC} = 1^{+-}$ would permit it to be quasi-diffractively produced(46). It is possible that this particle could be an as yet undiscovered vector meson.

We have also searched for the production of resonances with masses between 1.3 GeV and 2 GeV at t = -.2 $(GeV/c)^2$ and ~17 GeV photon energy. The low |t| value and high energy should be especially suitable for singling out states that could be diffractively produced. In particular we might have expected to observe any new vector mesons in this mass range such as the $J^{PC} = 1^{--}$ state on the "daughter" trajectory of the rho trajectory.

A single integral yield curve shows structure arising from both the high energy photoproduction of high mass states and from lower energy photon production of single pion or other low mass states. Therefore for this survey we used a subtraction of two sweeps taken at 17.8 GeV and 16 GeV peak energies. Fig. 19 shows both the unsubtracted and subtracted yields. The integral yield curves represent on the order of $2X10^7$ counts each. Any produced particle would show up as a peak in the subtracted yield curve. No such peak can be seen in the data. To determine the statistical significance level of this mass search we have made an

analysis of the data with the following method. A straight line (two parameters) was fitted to the subtracted yield curve. This fit, although expected to be poor in the region of masses just above the phi, gave a good representation of the data with a chi-square of 82 for 93 degrees of freedom. We then searched the subtracted yield curve for any significant peaks superimposed on this smooth linear fit. This was done by computing the ratio:

$$\frac{\Sigma_1 W_i (n,a) T_i}{\left(\Sigma_1 W_1^2 \sigma_i^2\right)^{1/2}} \qquad (7.1)$$

where T_i is the difference between the measured yield in mass bin "i" and the straight line fit, W_i is a Gaussian "weight function" centered in bin "n" with a full width at half maximum of "a", and σ_i is the error assigned to the measured point in bin "i". The above quantity was then centered on each bin and computed for several choices of "a" between 50 MeV to 250 MeV. For none of the large number of possible combinations was the above ratio larger than 3.0. We set our level of significance as 5 for this ratio. The resulting upper limits to the cross sections for widths of 100 MeV and 200 MeV are given in Table III.

We checked for internal consistency by searching the data for "negative" or non-physical inverted peaks. In this case the ratio was never larger than 2.5.

At the energy of 16.9 GeV the minimum four momentum transfer squared to the nucleon for the production of a meson as massive as 2 GeV is $-.014\ (GeV/c)^2$ and is small compared with the value of $t = -.2\ (GeV/c)^2$ at which the measurement was made.

Therefore there should be no inhibition on the production of a 2 GeV mass meson from this cause. It is possible that a high mass vector meson might escape observation in production experiments if it decayed into omega mesons and neutral pi mesons which would give final states containing two neutral pions. As this is a missing mass experiment our observations are completely independent of the decay modes open to the particle. We conclude from Table III that at a 90% confidence level no particle with a cross section larger than about 5% of the ρ^o cross section was produced in the mass region from 1.3 GeV to 2 GeV.

ACKNOWLEDGEMENTS

We are indebted to Dr. G. Fisher for the loan of the Cerenkov beam monitor and the calorimeter. Prof. M. Gettner and Prof. R. Prepost participated in the early stages of the experiment and gave us valuable support. We wish to thank Dr. F. Gilman for many helpful discussions. Four of us, W. G. Jones, D. Kreinick, F. Murphy and R. Weinstein, would like to thank W. K. H. Panofsky for hospitality extended to them by S.L.A.C. One of us, W. G. Jones would like to thank A. Tollestrup and the California Institute of Technology for hospitality extended to him. J. Grant, J. Escalera and J. Schroeder and Group C Technicians, M. Lateur and R. Culver gave us invaluable support with the setup and preparations for the experiment. We are indebted to the operations and support crews at the Stanford Linear Accelerator Center for their efficient operations and especially to R. Bell and A. Golde.

REFERENCES

1. R. Anderson et al., Phys. Rev. Letters 21, 384 (1968).
   W. G. Jones et al., Phys. Rev. Letters 21, 586 (1968).
2. M. Braunschweig et al., Phys. Letters 26B, 405 (1968).
3. G. C. Bolon et al., Phys. Rev. Letters 18, 926 (1967).
4. M. P. Locher and H. Rollnik, Phys. Letters 22, 696 (1966).
5. J. P. Ader, M. Capdeville and Ph. Salin, Nuclear Phys. B3, 407 (1967).
6. D. Bellenger et al., Phys. Rev. Letters 21, 1205 (1968).
7. F. M. Pipkin, Proceedings of the 1967 International Symposium on Electron and Photon Interactions at High Energies, Stanford Linear Accelerator Center, 1967.
8. S.C.C. Ting, Proceedings of the XIV International Conference on High Energy Physics, Vienna 1968.
9. G. McClellan et al., Phys. Rev. Letters 22, 374 (1969).
10. M. Davier et al., Phys. Rev. Letters 21, 841 (1968).
11. H. J. Lipkin, Phys. Rev. Letters 16, 1015 (1966).
    H. Joos, Phys. Letters 24B, 103 (1967).
    M. Davier, Phys. Rev. Letters 20, 952 (1968). The model was extended to finite values of t by B. Margolis, Nuclear Phys. B6, 687 (1968).
12. D.E.S.Y. Bubble Chamber Collaboration, Phys. Rev. 175, 1669 (1968).
    M. Davier et al., Phys. Letters 28B, 619 (1969).
13. K. Kajantie and J. S. Trefil, Phys. Letters 24B, 106 (1968).

14. E. Lohrmann, Proceedings of the 1967 International Symposium on Electron and Photon Interactions, Stanford Linear Accelerator Center, 1967.

15. R. L. Anderson, Nuclear Instr. and Methods 70, 87 (1969).

16. R. L. Anderson et al., Nuclear Instr. and Methods 66, 328 (1968).

17. R. L. Anderson and D. Porat, Nuclear Instr. and Methods 70, 77 (1969).

18. Chronetics, Inc., Mount Vernon, New York.

19. Transistor Specialties Incorporated, Terminal Drive, Plainview, L.I., New York.

20. R. L. Anderson, Nuclear Instr. and Methods 65, 195 (1968).

21. G. Fisher and Y. Murata, SLAC-PUB-605 (May, 1969) (to be submitted to Nuclear Instr. and Methods).

22. D. L. Kreinick, High Energy Photoproduction of Neutral Mesons, Doctoral Thesis, California Instit. of Tech., Pasadena, Calif.

23. D. Caldwell et al., (Private Communication).

24. G. Höhler et al., Phys. Letters 20, 79 (1966).

25. D. Bellenger, et al., Contribution to the XIV International Conference on High Energy Physics, Vienna (1968).

26. A. Capella and J. Tran Thanh Van, Nuovo Cimento Letters 1, 321 (1969).

27. A. P. Contogouris and J. P. Lebrun, Preprint, Institute of Theoretical Physics, McGill University, Montreal, Canada, May 1969.

28. J. Fröyland, Nucl. Phys. B11, 204 (1969).

29. M. L. Blackmon et al., Argonne National Laboratory Report 69-514 (1969).

30. Private Communication - L. Jones, Cal-Tech., c.f. for general discussion of fixed poles in photoproduction see:

S. Mandelstam and Wang, Phys. Rev. 160, 1490 (1967).

31. A. Dar et al., Phys. Rev. Letters 20, 1261 (1968).

32. F. Henyey et al., Phys. Rev. Letters 21, 946 (1968).

33. A. Dar and V. F. Weisskopf, Phys. Rev. Letters 20, 762 (1968).

34. B. Gorczyca and M. Hayashi - Preprint, Institute of Theoretical Physics, Jagellonian University, Cracow, Poland.

35. J. D. Jackson, Nuovo Cimento 34, 1644 (1964).

F. Selleri, Phys. Letters 3, 76, (1962).

36. M. Ross and L. Stodolsky, Phys. Rev. 149, 1172 (1966).

37. P. Söding, Phys. Letters 19, 702 (1966).

38. Aachen-Berlin-Bonn-Hamburg-Heidelberg-Munchen collaboration, Phys. Letters 27B, 54 (1968).

39. c.f., for instance S.D. Drell and J. S. Trefil, Phys. Rev. Letters 16, 552 (1966), in which the angular dependence of ρ^{o} meson photoproduction on complex nuclei is obtained without any explicit reference to the assumptions of a strict Vector Dominance theory.

40. K. J. Foley, Phys. Rev. Letters 11, 425 (1963).

41. F. Bulos, Phys. Rev. Letters 22, 490 (1969), c. f. see also Asbury et al., Phys. Rev. Letters 19, 865 (1967) for values

42. G. McClellan, Phys. Rev. Letters 22, 377 (1969).

43. Relation (6.2) is not the relation usually quoted in the literature (11). The generally quoted relation is:

$$\sigma_T(\varphi p) = 2\,\sigma_T(K^+p) + \sigma_T(\pi^-p) - 2\,\sigma_T(\pi^+p)$$

This relation makes use of an additional assumption based on the Pomeranchuk theorem to eliminate the use of K^-p cross sections.

44. K. J. Foley et al., Phys. Rev. Letters 11, 503 (1963).
K. J. Foley et al., Phys. Rev. Letters 15, 45 (1965).

45. R. J. Oakes and J. J. Sakurai, Phys. Rev. Letters 19, 1266 (1967). This is now the most generally accepted derivation of this ratio. References to the many earlier papers on this ratio can be found in the above reference.

46. D. R. O. Morrison, Phys. Letters 22, 528 (1966).

TABLE I

CORRECTIONS AND NORMALIZATION UNCERTAINTIES IN PERCENT

CORRECTION \ $-t(GeV/c)^2$	.12	.2	.3	.4	.5	.7	.9	1.1	1.4
Acceptance Correction* due to energy losses in the target	18.7 ± 1	7.5 ± 0.4	3.3 ± 0.2	1.9 ± 0.1	1.4 ± 0.1	0.7 ± 0.1	- negligible -		
Proton losses (due to vetoing by the C_π counter)		1 ± 0.5	1 ± 0.5	1 ± 0.5	1 ± 0.5	1 ± 0.5	1.5 ± 0.5	2.8 ± 1.0	5.8 ± 1.5
Hodoscope counter inefficiency	3 ± 1	5 ± 2	5 ± 2	5 ± 2	5 ± 2	5 ± 2	5 ± 2	5 ± 2	5 ± 2
Nuclear absorption losses of protons	9 ± 3	5 ± 1	11 ± 2	9 ± 2	8 ± 2	8 ± 2	8 ± 2	8 ± 3	8 ± 3
Solid Angle Calibration of the Spectrometer	± 3	± 3	± 3	± 3	± 3	± 3	± 3	± 3	± 3
Beam Monitor** Calibration	± 2	± 2	± 2	± 2	± 2	± 2	± 2	± 2	± 2
Rate Dependence	0 - 5%, with an uncertainty of ± 2%								
Net overall normalization uncertainty	5.3	4.8	5.0	5.0	5.0	5.0	5.0	5.5	5.7

*The spread in dP/P changes as a group of particles loses energy in traversing the target.

**Includes the uncertainty in the 3% correction for photons converted before reaching the target, and the estimated uncertainties in the calculated bremsstrahlung spectrum.

TABLE II

Forward differential and total ρ cross sections obtained from fits to our data calculated both with a best fit constant C_ρ from Equation 5.3 and calculated with an energy dependent C_ρ best fitted at each energy.

E_o	CONSTANT C_ρ		ENERGY DEPENDENT C_ρ		
	$d\sigma/dt(t=0)$	σ_T	$d\sigma/dt(t=0)$	σ_T	% error
17.8	104.6	12.39	100.5	11.89	+ 5%
16.9	105.3	12.47	105.3	12.47	+ 6%
16.0	105.9	12.55	103.3	12.24	+ 6%
15.25	106.7	12.65	106.6	12.54	+ 6%
14.5	107.6	12.74	101.2	11.98	+ 6%
13.75	108.8	12.87	109.5	12.95	+ 5%
13.0	110.1	13.04	108.7	12.86	+ 6%
12.25	111.6	13.23	111.4	13.19	+ 6%
11.5	113.4	13.44	113.4	13.44	+ 6%
6.5	131.0	15.50	137.6	16.27	+ 10%
6.0	133.3	15.79	151.9	18.0	+ 10%
5.5	135.8	16.09	166.9	19.8	+ 12%

TABLE III

Upper limits to cross sections in the missing mass search at 16.9 GeV average photon energy and $t = -0.2$ $(GeV/c)^2$ for the production of particles with widths 100 MeV and 200 MeV.

Mass, MeV	100 MeV Width		200 MeV Width	
	Upper limit for $(\frac{d\sigma}{dt})$, $\frac{\mu b}{(GeV/c)^2}$	Upper limit for $\frac{d\sigma}{dt}/\frac{d\sigma}{dt}(\rho)$	Upper limit for $(\frac{d\sigma}{dt})$, $\frac{\mu b}{(GeV/c)^2}$	Upper limit for $\frac{d\sigma}{dt}/\frac{d\sigma}{dt}(\rho)$
1300	0.49	.022	0.69	.031
1450	0.54	.024	0.76	.034
1600	0.61	.028	0.87	.039
1800	0.71	.032	1.00	.045

FIGURE CAPTIONS

Fig. 1: Experimental Arrangement.

Fig. 2: Positioning of the spectrometer and the counters relative to the beam line and the target. The insert shows the detector system in more detail.

Fig. 3: Block diagram of the electronics. Only the main logic is shown.

Fig. 4: Kinematics for photoproduction of various mesons for a incident photon energy of 11.5 GeV. Plotted is the momentum of the recoil proton versus its laboratory angle for π^o, η, ρ^o, and φ production. Note that for a fixed momentum the laboratory angle is nearly proportional to missing mass squared.

Fig. 5: A) The measured proton yield for a peak bremsstrahlung energy of 11.5 GeV and for $t = -.7$ $(GeV/c)^2$. The ordinate is the number of protons per hodoscope counter per 10^{11} E.Q. The abscissa represents $(mm)^2$ in GeV^2. The steps due to the onset of π^o, ρ^o, and φ production are clearly seen. The solid line through the data points represents a least square fit to the data assuming π^o, ρ^o, and φ production in addition to nonresonant background. The breakdown of the yield into the separate contributions is also shown.

B) The subtracted proton yield curve in counts per hodoscope counter per 10^{11} E.Q. for photons between 13.0 GeV and 11.5 GeV and for $t = -.7$ $(GeV/c)^2$. This curve was obtained by subtracting the 11.5 GeV proton yield from the corresponding proton yield at 13 GeV end-point energy. The peaks due to π^o, ρ^o,

and φ production are again clearly seen. Due to multiple scattering of the recoil proton in traversing the target the η is not clearly resolved from the ρ^o peak.

C) The differential yield curve derived from the integral curve in 5A. Plotted is the difference, in counts per 10^{11} E.Q., between once removed yield points versus missing mass squared. Note the close similarity to the subtracted yield curve in Fig. 5B.

Fig. 6: A) The measured proton yield in counts per hodoscope element per 10^{11} E.Q. is plotted versus missing mass squared in the region around the π^o step for an photon end-point energy of 6 GeV and for $t = -1.1$ $(GeV/c)^2$.

B) The differential yield curve derived from the integral yield in Fig. 6A. Plotted is the difference in counts per 10^{11} E.Q. between once removed yield points versus missing mass squared.

Fig. 7: $d\sigma/dt$ in $\mu b/(GeV/c)^2$ versus t for the reaction $\gamma + P \rightarrow \pi^o + P$ at incident photon energies of 6, 9, 12, and 15 GeV. The lines drawn through the data are only to guide the eye.

Fig. 8: $s^2\, d\sigma/dt$ in $\mu b\ (GeV)^2$ is plotted versus t for the reaction $\gamma + P \rightarrow \pi^o + P$. Plotted is the 6 GeV data together with data from D.E.S.Y. at 5 GeV and 5.8 GeV. Data in the Primakoff region have been excluded.

Fig. 9: $d\sigma/dt$ in $\mu b/(GeV/c)^2$ for fixed t is plotted versus $(s-m^2)$. Shown is the data from this experiment as well as data

at lower energies from D.E.S.Y. The solid line is a least squares fit to the data of the form $d\sigma/dt \sim (s-m^2)^{2\alpha-2}$. The value of α is listed for each |t| value.

Fig. 10: A) The measured proton yield in the vicinity of the step is plotted versus missing mass squared for an end-point bremsstrahlung energy of 5.5 GeV and t = -.5 $(GeV/c)^2$. The ordinate is counts per hodoscope element per 10^{11} E.Q.

B) The differential curve derived from the integral yield curve in 10A. Plotted is the difference in counts per 10^{11} E.Q. between once removed yield points versus missing mass squared.

Fig. 11: $s^2\ d\sigma/dt$ in $\mu b\ (GeV)^2$ is plotted versus t for the reaction $\gamma + P \rightarrow \eta + P$ for photon energies between 5.5 GeV and 9 GeV. The dotted line shows the π^o cross section at 6 GeV for comparison purposes.

Fig. 12: The results of this experiment are compared with the results of an experiment at C.E.A. at 4 GeV. Plotted is $s^2\ d\sigma/dt$ in $\mu b\ (GeV)^2$ versus t. The dotted line is the cross section predicted by Dar and Weisskopf using vector dominance and assuming only ρ exchange. The solid line is a prediction by Gorczyca and Hayashi based on vector dominance but allowing ω and B exchange in addition to ρ exchange. The two predictions assumed different values for the coupling constant $g_{\omega\gamma}$.

Fig. 13: A) The measured proton yield per hodoscope element per 10^{11} E.Q. is plotted versus missing mass squared for an end-point bremsstrahlung energy of 16 GeV and t = -.7 $(GeV/c)^2$.

The positions of the steps due to the onset of π^o, ρ, and φ production are indicated.

B) The differential yield curve obtained from the integral yield curve in Fig. 13A is shown. Plotted is the difference in counts between once removed points per 10^{11} E.Q. The peaks due to π^o, ρ^o, and φ production are clearly seen.

C) The subtracted proton yield curve in counts per hodoscope counter per 10^{11} E.Q. for photons between 17.8 GeV and 16 GeV and t = -.7 $(GeV/c)^2$ is plotted versus missing mass squared. This curve was obtained by subtracting the 16 GeV proton yield from the corresponding yield at 17.8 GeV end-point energy. The solid line through the data points represents a least square fit assuming π^o, ρ^o, and φ production in addition to nonresonant background. The breakdown of the yield into the separate contributions is shown as dotted lines.

Fig. 14: $d\sigma/dt$ in $\mu b/(GeV/c)^2$ is plotted versus t for the reaction $\gamma + P \rightarrow \rho^o + P$ for photon energies between 5.5 GeV and 6.5 GeV. The solid line is a least squares fit by the D.E.S.Y. bubble chamber group to their data for photon energies between 4.5 and 5.8 GeV. Acceptable limits to their fits are indicated by the dotted lines. The results of a measurement at Cornell(9) for an end-point energy of 6 GeV are also shown.

Fig. 15: $d\sigma/dt$ in $\mu b/(GeV/c)^2$ versus t, for the reaction $\gamma + P \rightarrow \rho^o + P$ at incident photon energies from 6.5 to 17.8 GeV. The lines drawn through the data points are a best fit to the quark relation in Eq.(5.2). The one adjustable parameter C_p

was set to a value of 2.98×10^{-3}.

Fig. 16: A) The measured proton yield in counts per hodoscope element per 10^{11} E.Q. is plotted versus missing mass squared in the region around the φ step for an incident photon energy of 14.5 GeV and for $t = -.4$ $(GeV/c)^2$.

B) The differential yield curve derived from the above integral curve is shown. Plotted is the difference in counts between once removed hodoscope elements per 10^{11} E.Q. versus missing mass squared.

Fig. 17: $d\sigma/dt$ in $\mu b/(GeV/c)^2$ versus t for the reaction $\gamma + P \rightarrow \varphi + P$ at incident photon energies between 6 GeV and 17.8 GeV. At 6 GeV we have included the D.E.S.Y. bubble chamber results(33) and the result at $t = 0$ of Asbury et al.(8). The solid line is a best fit to the quark relations (6.1) and (6.2) with the one adjustable parameter C_φ set to 18.6×10^{-5}.

Fig. 18: The subtracted proton yield per hodoscope element per 10^{11} E.Q. is plotted versus missing mass squared for photons between 14.5 and 13 GeV. The peaks due to ρ^0 and φ production can be seen. In addition the curve shows a particle with mass of about 1250 MeV ("B") being produced with roughly the same cross section as the φ. The solid curve is a least squares fit to the data assuming π^0, ρ^0, φ and the "B" meson in addition to a smoothly varying amount of background. The relative contributions are indicated in the figure.

Fig. 19: Shown are the results of a mass search in the region of missing mass squared of 1.5 $(GeV)^2$ to 4 $(GeV)^2$ for

$t = -.2$ $(GeV/c)^2$. Plotted is the proton yield per hodoscope element per 10^{11} E.Q. as a function of missing mass squared for end-point energies of the bremsstrahlung spectrum of 17.8 and 16 GeV respectively. The structure seen in these curves was due to low energy single π^o production. The upper scale shows the photon energy responsible for single π^o production. The prominent bumps are associated with the third and fourth resonances. The subtraction between the two properly normalized yield curves then corresponds to reactions initiated by photons between 17.8 and 16 GeV. The result of this subtraction is shown in the figure on an expanded scale. The solid line is a least squares fit of a straight line to the data.

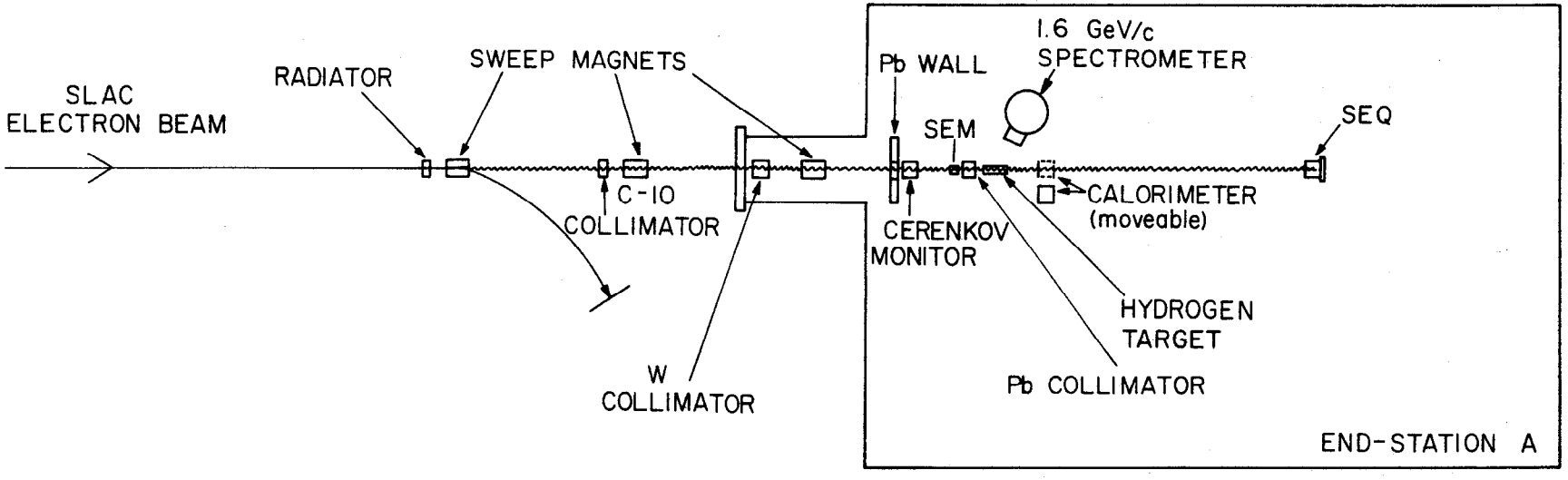
SLAC
ELECTRON BEAM
RADIATOR
SWEEP MAGNETS
C-10
COLLIMATOR
W
COLLIMATOR
Pb WALL
1.6 GeV/c
SPECTROMETER
SEM
SEQ
CERENKOV
MONITOR
CALORIMETER
(moveable)
HYDROGEN
TARGET
Pb COLLIMATOR
END-STATION A
0
25
50
75
SCALE IN FEET

Fig. 1

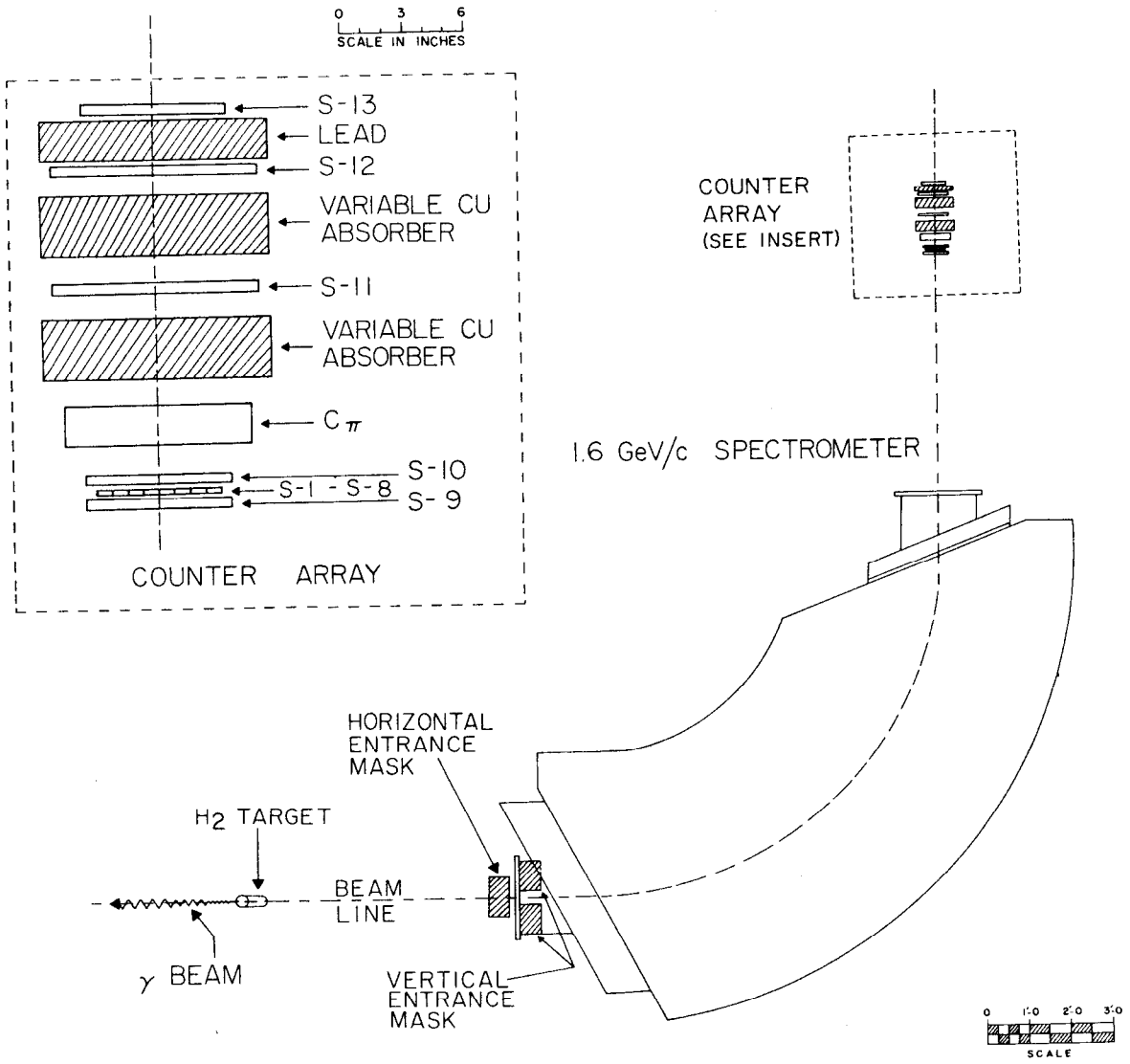
0 3 6
SCALE IN INCHES
S-13
LEAD
S-12
VARIABLE CU ABSORBER
S-11
VARIABLE CU ABSORBER
C_π
S-10
S-1 - S-8
S-9
COUNTER ARRAY
COUNTER ARRAY (SEE INSERT)
1.6 GeV/c SPECTROMETER
HORIZONTAL ENTRANCE MASK
H_2 TARGET
BEAM LINE
γ BEAM
VERTICAL ENTRANCE MASK
0 1·0 2·0 3·0
SCALE

Fig. 2

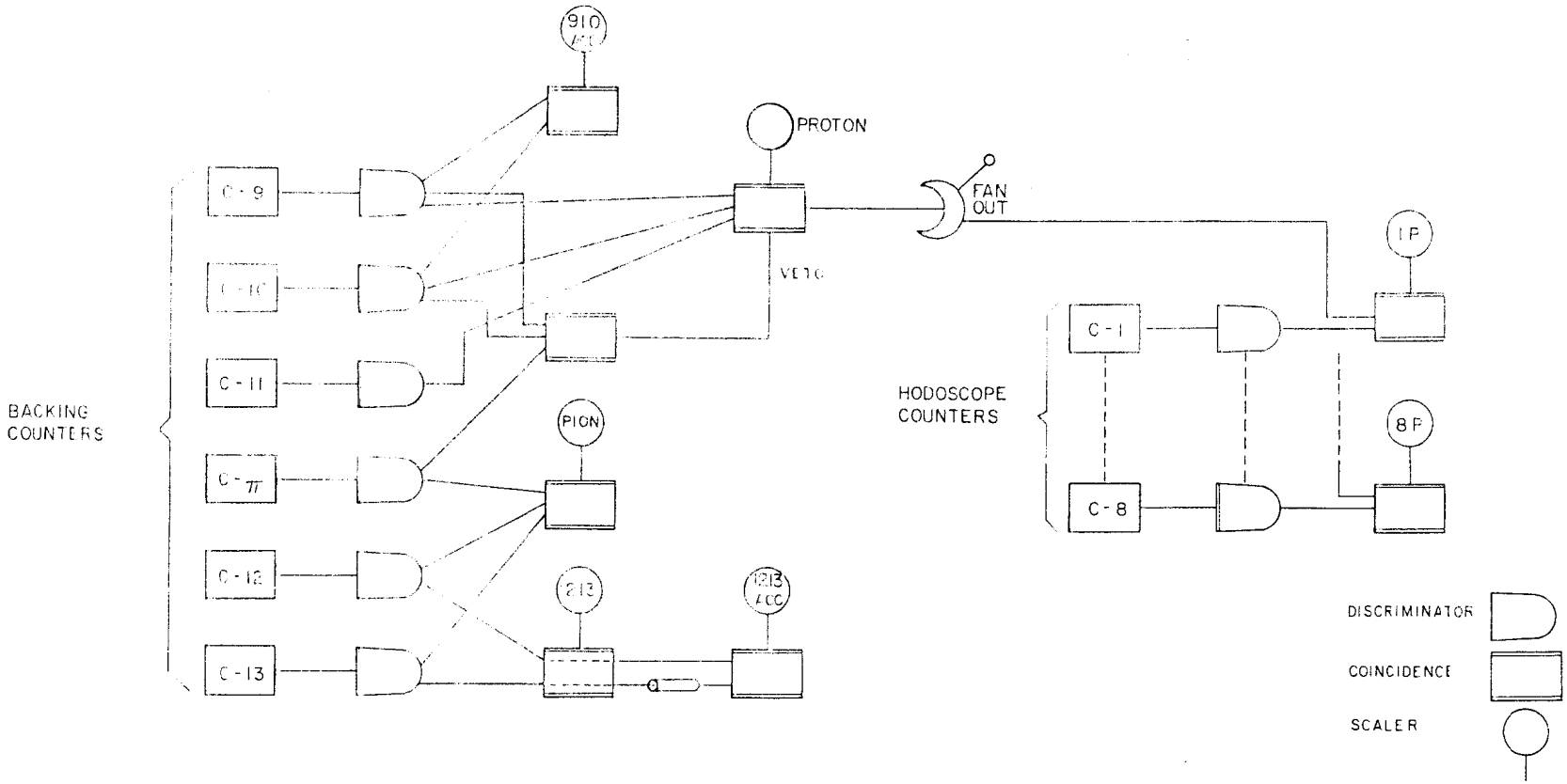
910
ACC
PROTON
FAN
OUT
C - 9
C - 10
C - 11
C - π
C - 12
C - 13
VETO
BACKING
COUNTERS
PION
2 3
1 2 3
ACC
1 P
C - 1
8 P
C - 8
HODOSCOPE
COUNTERS
DISCRIMINATOR
COINCIDENCE
SCALER

Fig. 3

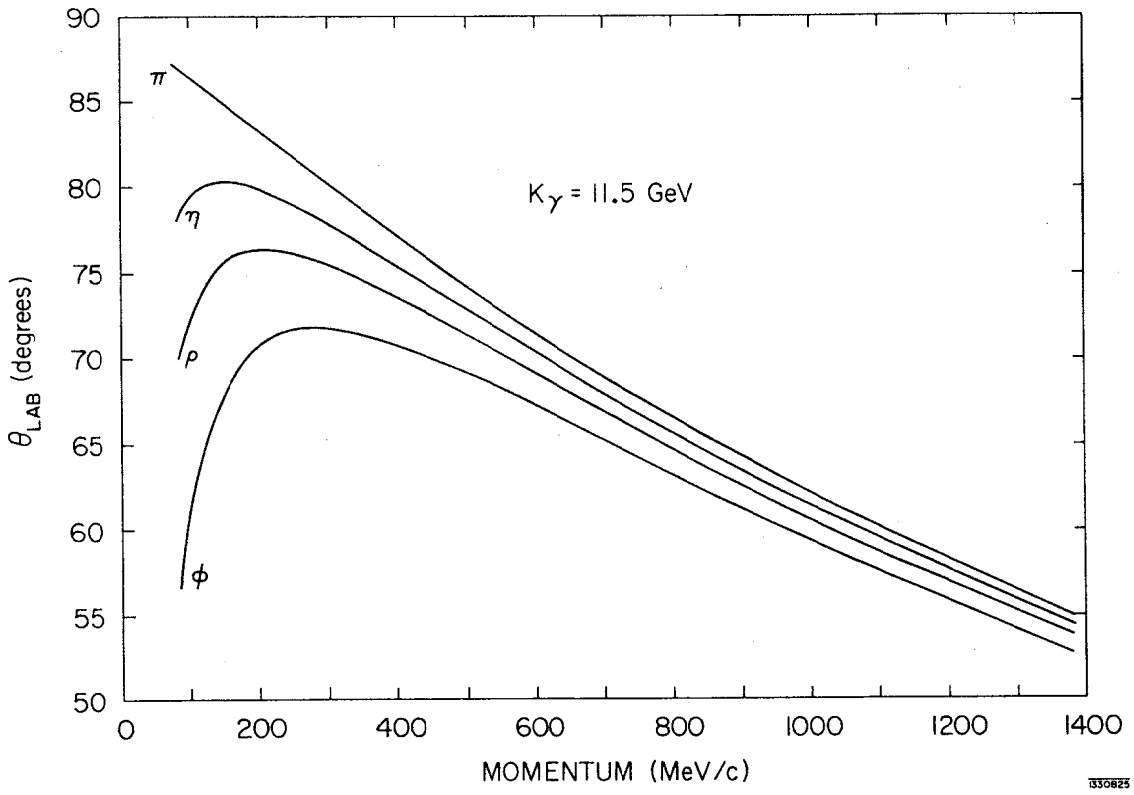
90
85
80
75
70
65
60
55
50
0
200
400
600
800
1000
1200
1400
θ_{LAB} (degrees)
MOMENTUM (MeV/c)
K_γ = 11.5 GeV
π
η
ρ
ϕ
330825

Fig. 4

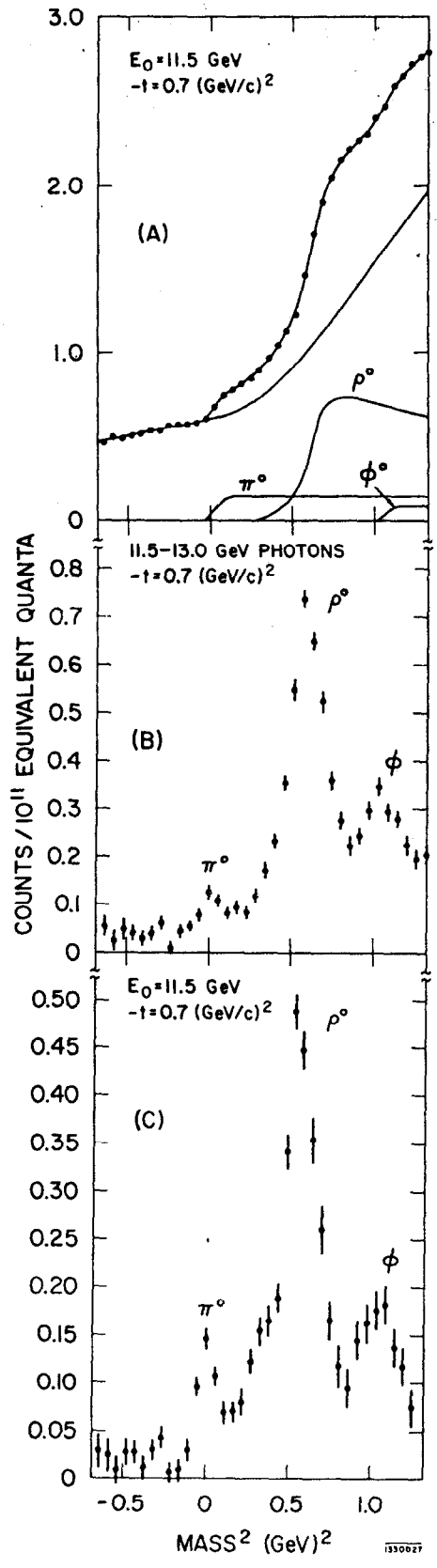
3.0
2.0
1.0
0
E_0=11.5 GeV
-t=0.7 (GeV/c)^2
(A)
ρ°
π°
ϕ°
11.5–13.0 GeV PHOTONS
-t=0.7 (GeV/c)^2
(B)
ρ°
ϕ
π°
0.8
0.7
0.6
0.5
0.4
0.3
0.2
0.1
0
E_0=11.5 GeV
-t=0.7 (GeV/c)^2
(C)
ρ°
ϕ
π°
0.50
0.45
0.40
0.35
0.30
0.25
0.20
0.15
0.10
0.05
0
COUNTS / 10^{11} EQUIVALENT QUANTA
-0.5
0
0.5
1.0
MASS^2 (GeV)^2
1330027

Fig. 5

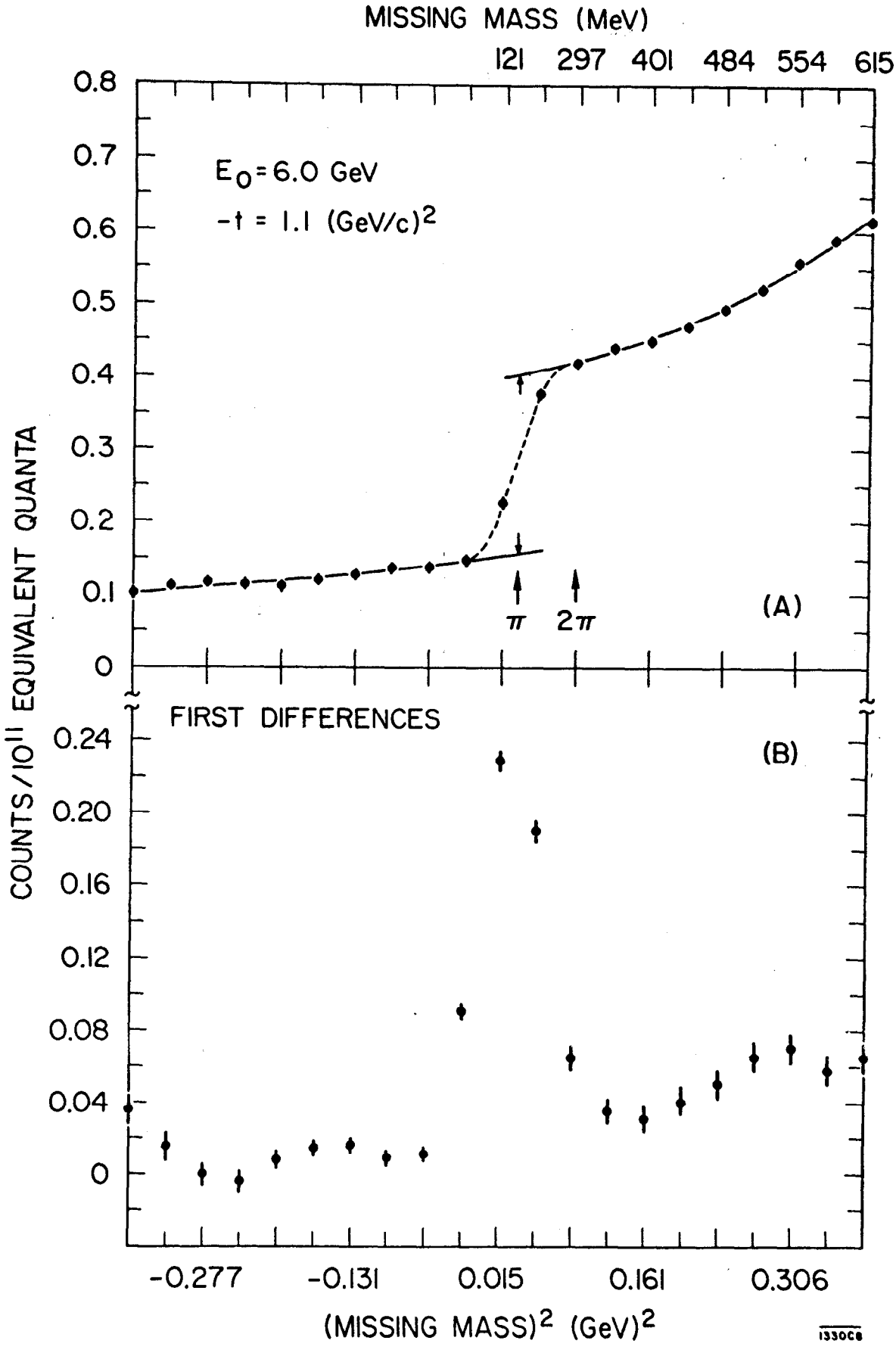
MISSING MASS (MeV)
121 297 401 484 554 615
0.8
0.7
0.6
0.5
0.4
0.3
0.2
0.1
0
E_0 = 6.0 GeV
$-t$ = 1.1 (GeV/c)^2
π
2π
(A)
COUNTS/10^{11} EQUIVALENT QUANTA
FIRST DIFFERENCES
(B)
0.24
0.20
0.16
0.12
0.08
0.04
0
-0.277
-0.131
0.015
0.161
0.306
(MISSING MASS)^2 (GeV)^2
133OC8

Fig. 6

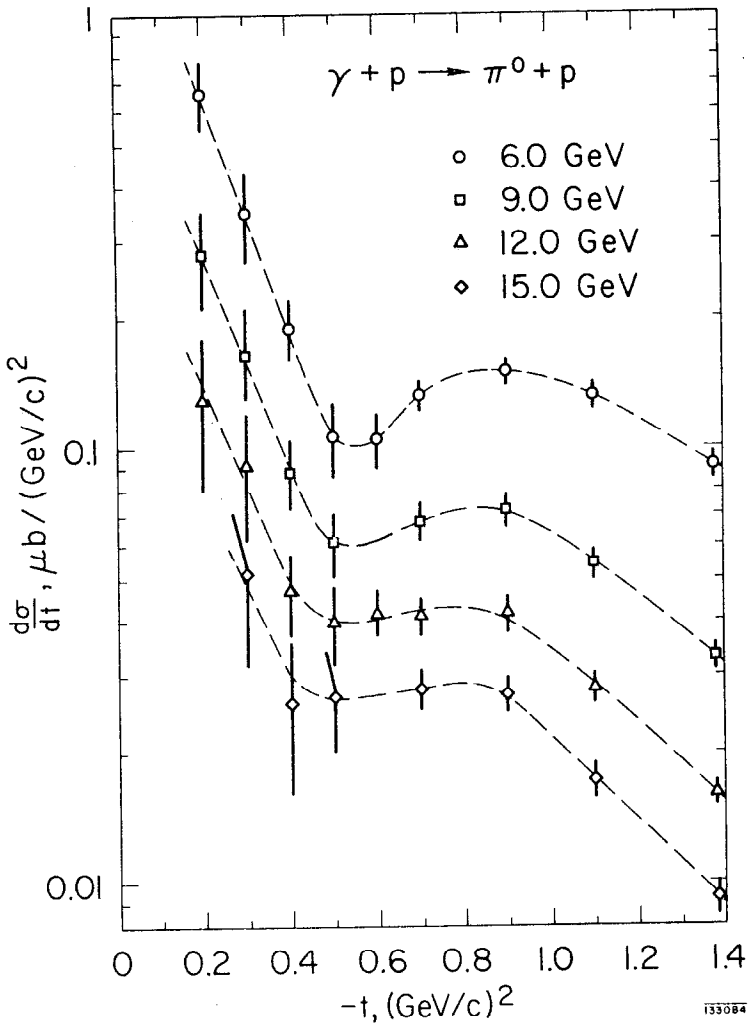
$\gamma + p \rightarrow \pi^0 + p$
6.0 GeV
9.0 GeV
12.0 GeV
15.0 GeV
$\frac{d\sigma}{dt}$, $\mu b / (GeV/c)^2$
1
0.1
0.01
0
0.2
0.4
0.6
0.8
1.0
1.2
1.4
$-t, (GeV/c)^2$
133084

Fig. 7

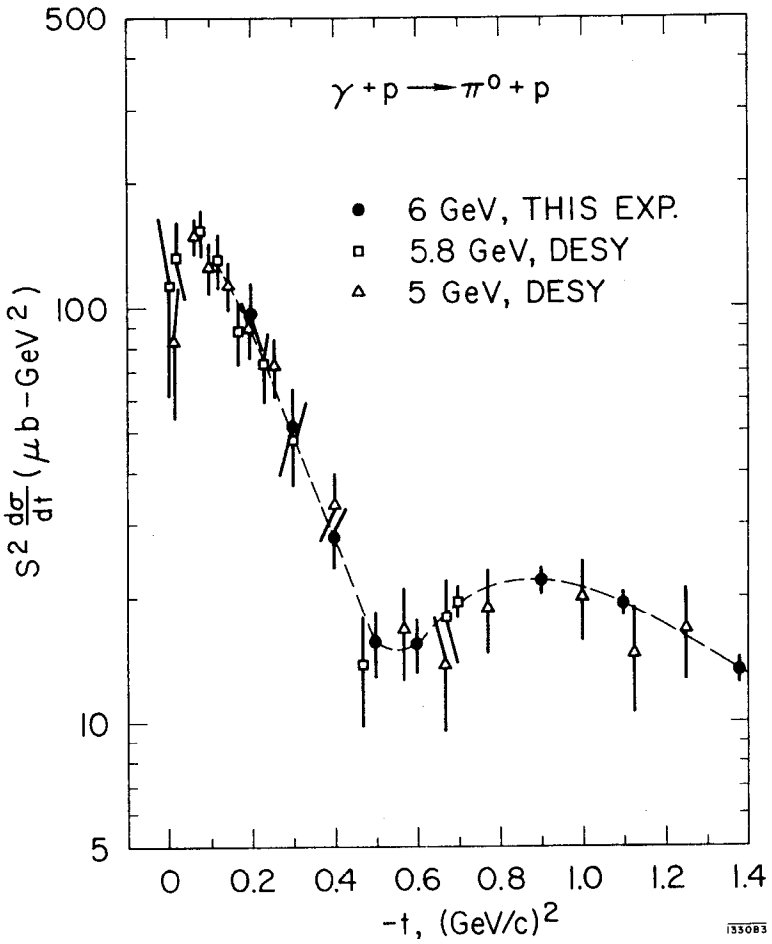
500
100
10
5
$\gamma + p \rightarrow \pi^0 + p$
6 GeV, THIS EXP.
5.8 GeV, DESY
5 GeV, DESY
$S^2 \frac{d\sigma}{dt}$ (μb-GeV^2)
0
0.2
0.4
0.6
0.8
1.0
1.2
1.4
-t, (GeV/c)^2
133083

Fig. 8

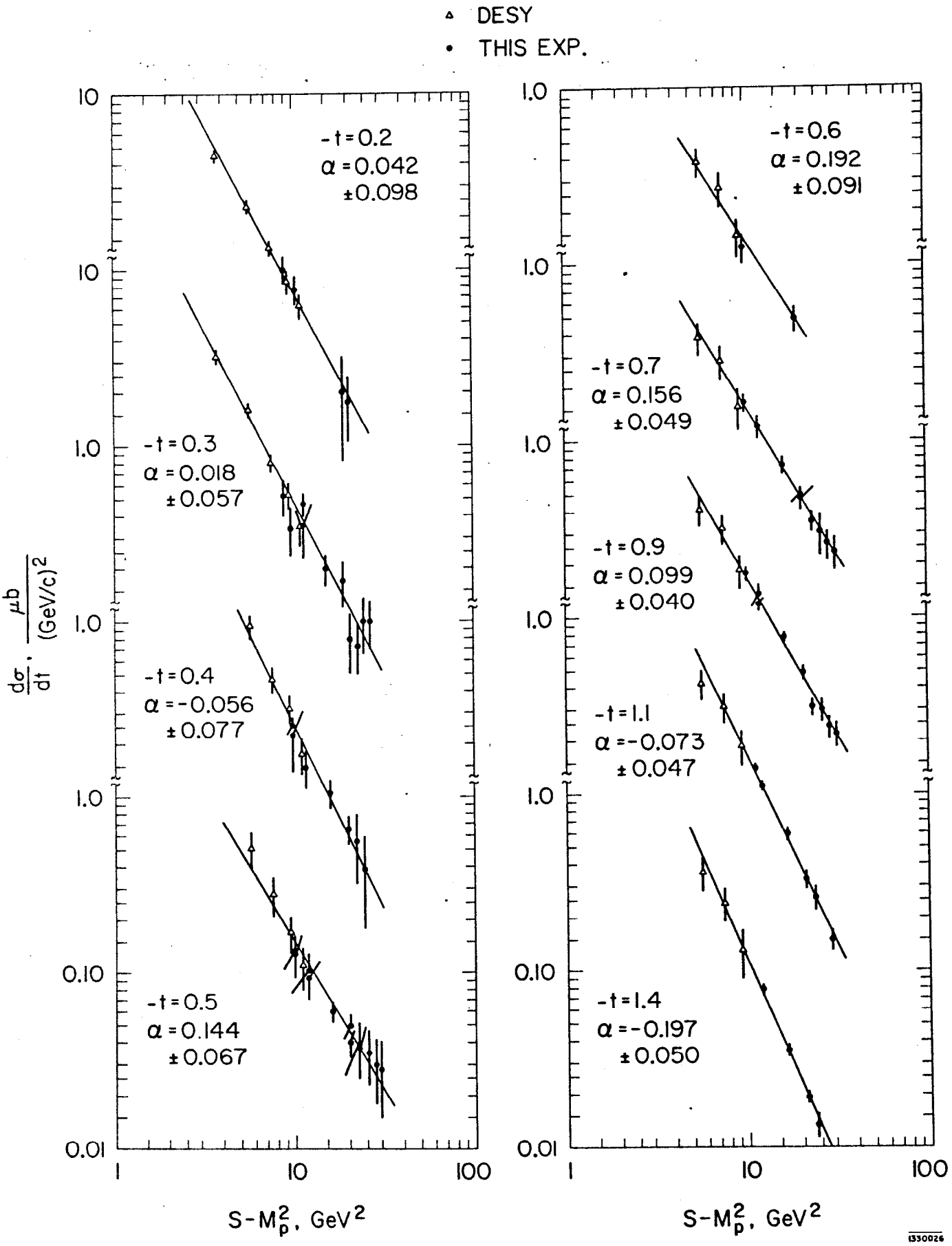
△ DESY
• THIS EXP.
-t=0.2
α=0.042
±0.098
-t=0.3
α=0.018
±0.057
-t=0.4
α=-0.056
±0.077
-t=0.5
α=0.144
±0.067
-t=0.6
α=0.192
±0.091
-t=0.7
α=0.156
±0.049
-t=0.9
α=0.099
±0.040
-t=1.1
α=-0.073
±0.047
-t=1.4
α=-0.197
±0.050
dσ/dt, μb/(GeV/c)²
S-M²p, GeV²
S-M²p, GeV²
1330026

Fig. 9

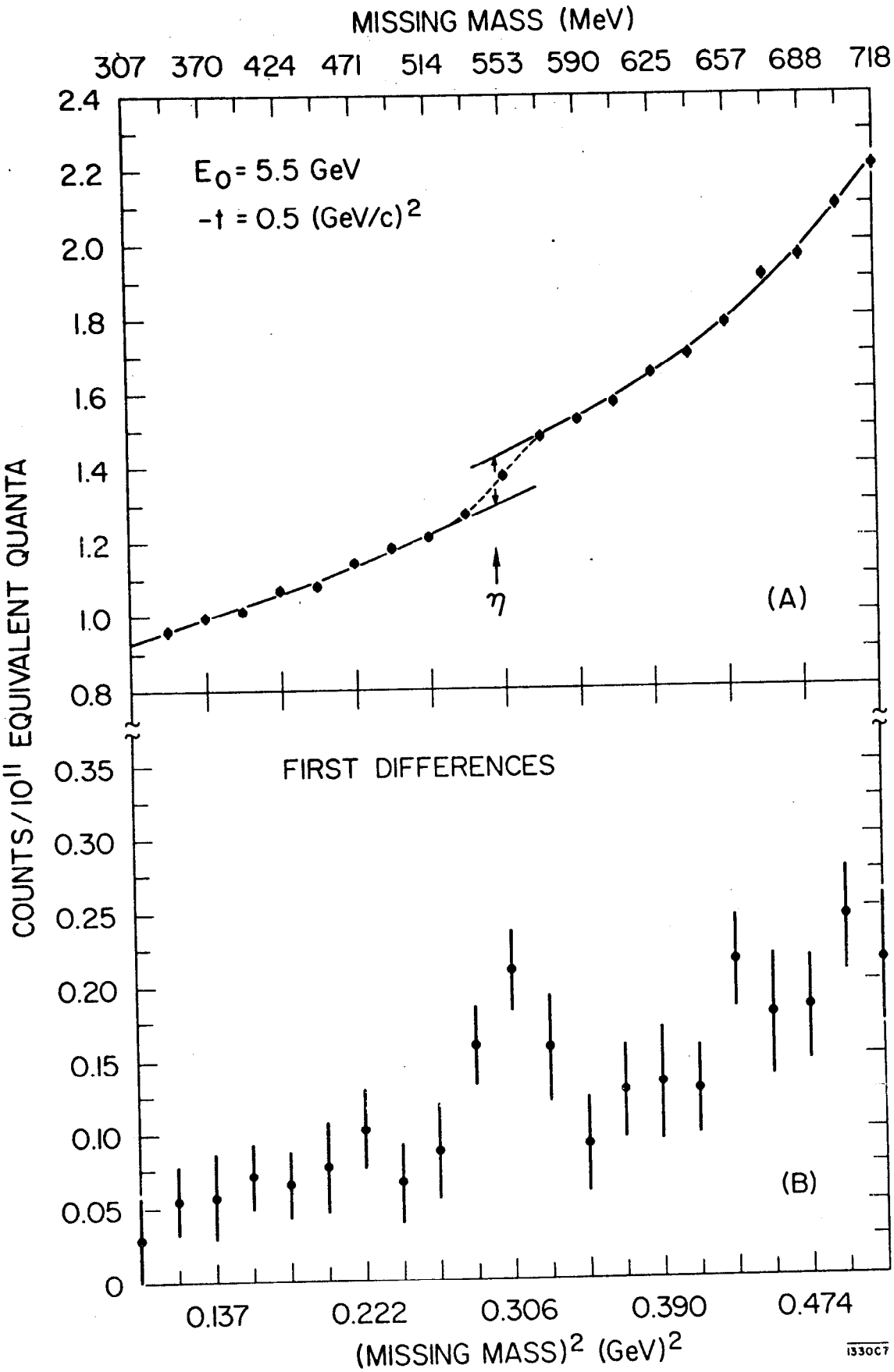
MISSING MASS (MeV)
307 370 424 471 514 553 590 625 657 688 718
2.4
2.2
2.0
1.8
1.6
1.4
1.2
1.0
0.8
E_0 = 5.5 GeV
$-t$ = 0.5 (GeV/c)^2
η
(A)
COUNTS/10^{11} EQUIVALENT QUANTA
FIRST DIFFERENCES
0.35
0.30
0.25
0.20
0.15
0.10
0.05
0
(B)
0.137
0.222
0.306
0.390
0.474
(MISSING MASS)^2 (GeV)^2
133007

Fig. 10

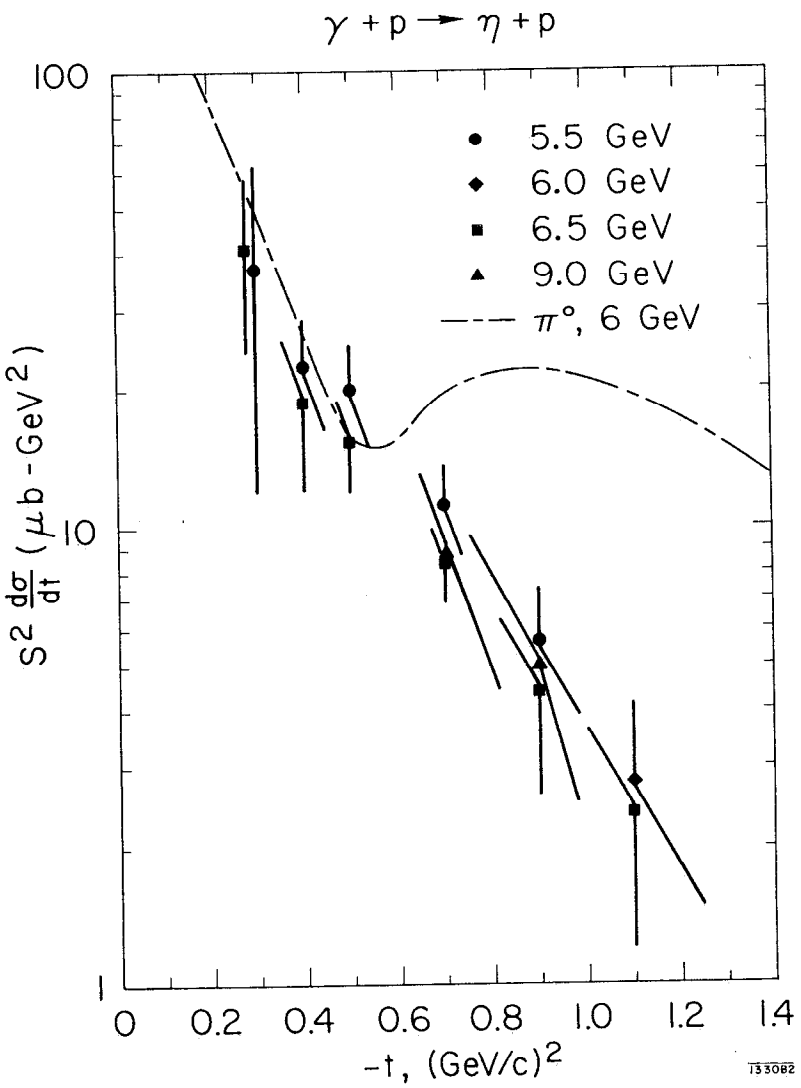
$\gamma + p \rightarrow \eta + p$
100
10
1
$S^2 \frac{d\sigma}{dt}$ (μb - GeV^2)
5.5 GeV
6.0 GeV
6.5 GeV
9.0 GeV
π°, 6 GeV
0
0.2
0.4
0.6
0.8
1.0
1.2
1.4
-t, (GeV/c)^2
133082

Fig. 11

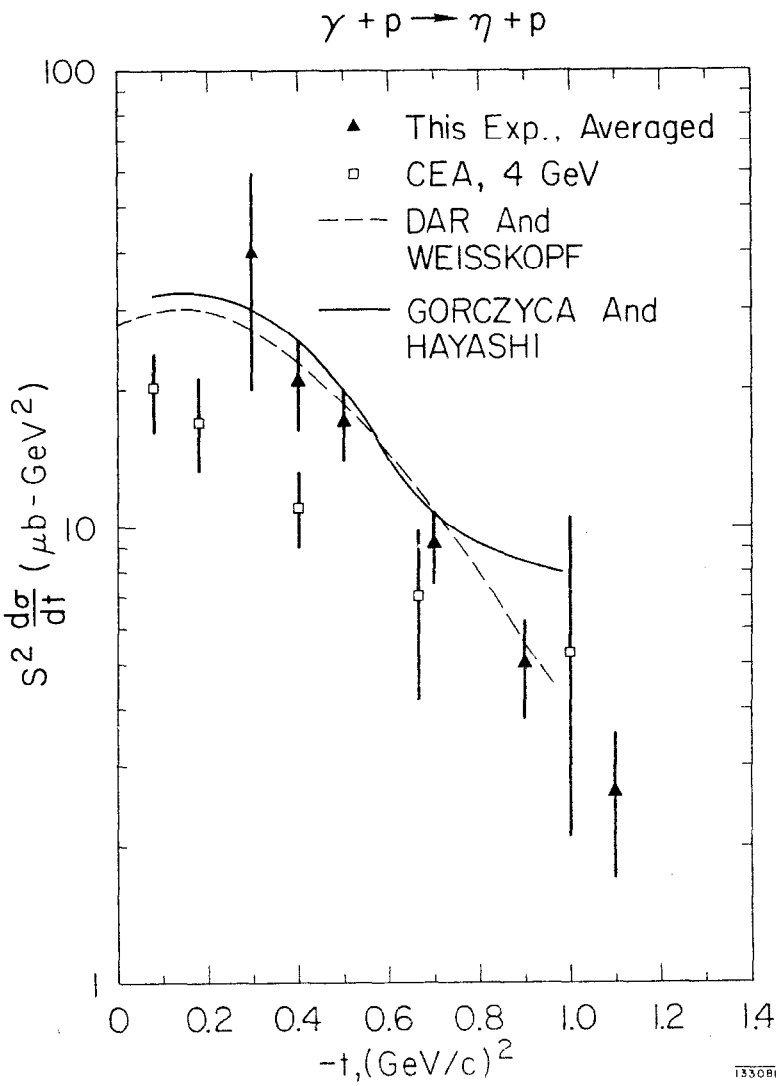
$\gamma + p \rightarrow \eta + p$
100
10
1
This Exp., Averaged
CEA, 4 GeV
DAR And WEISSKOPF
GORCZYCA And HAYASHI
$S^2 \frac{d\sigma}{dt}$ (μb - GeV^2)
0
0.2
0.4
0.6
0.8
1.0
1.2
1.4
$-t$,(GeV/c)^2
133081

Fig 12

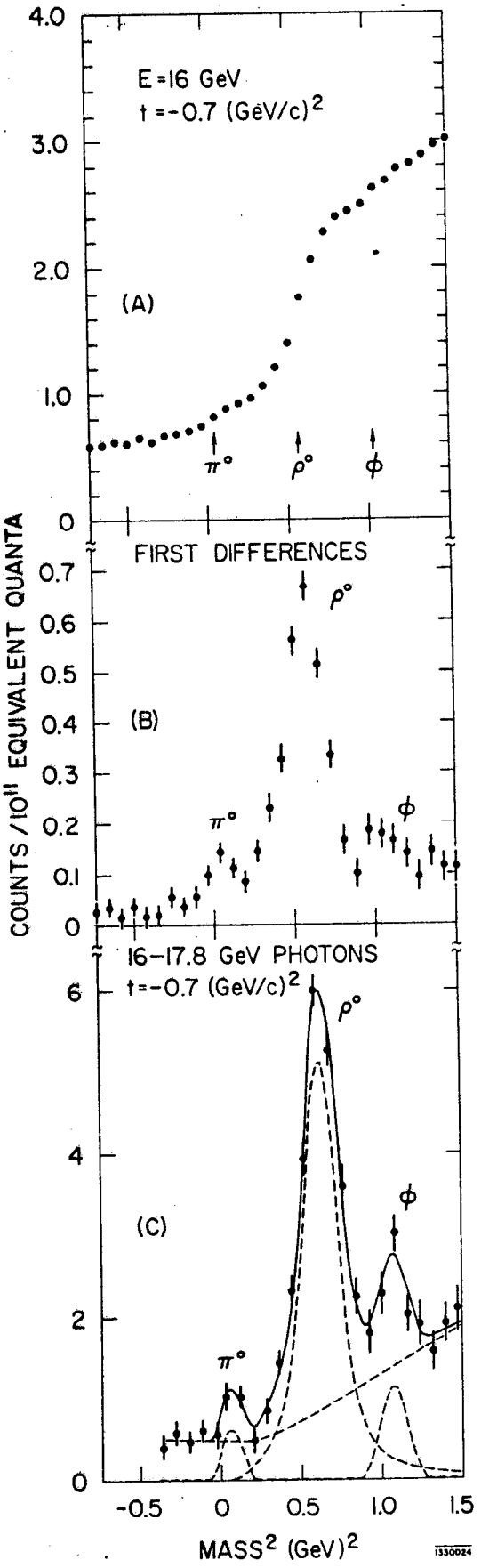
E=16 GeV
t=-0.7 (GeV/c)²
(A)
π°
ρ°
φ
FIRST DIFFERENCES
(B)
COUNTS/10¹¹ EQUIVALENT QUANTA
16-17.8 GeV PHOTONS
t=-0.7 (GeV/c)²
(C)
MASS² (GeV)²
1330024

Fig. 13

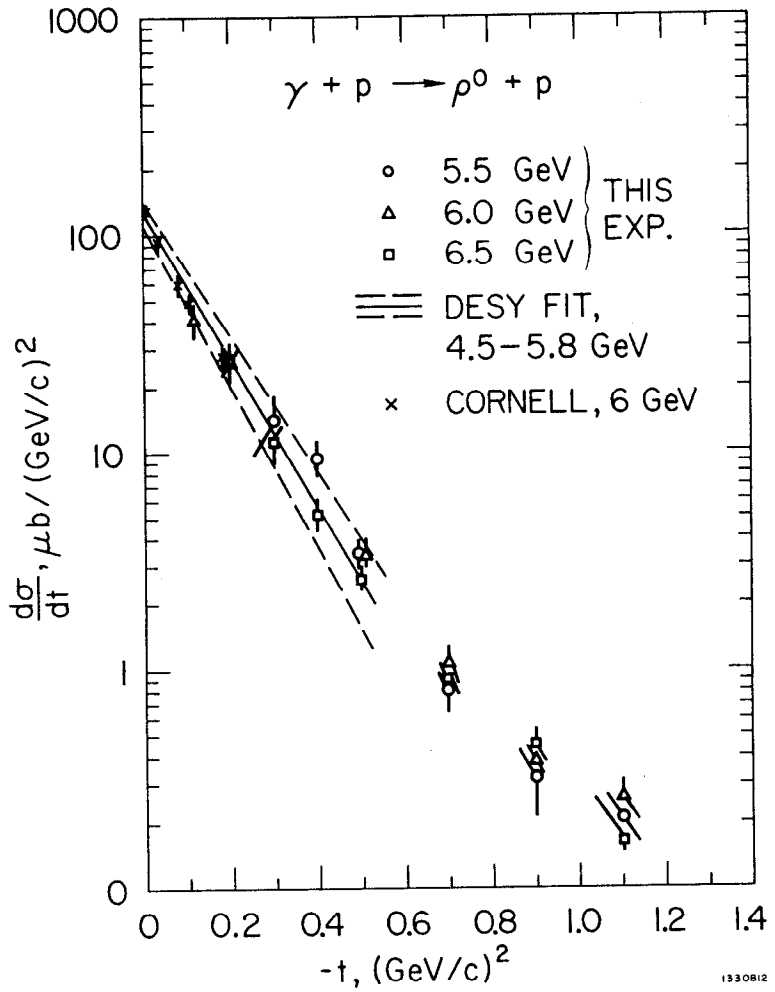
1000
100
10
1
0
$\gamma + p \rightarrow \rho^0 + p$
5.5 GeV
6.0 GeV
6.5 GeV
THIS EXP.
DESY FIT, 4.5–5.8 GeV
CORNELL, 6 GeV
$\frac{d\sigma}{dt}, \mu b/(GeV/c)^2$
0
0.2
0.4
0.6
0.8
1.0
1.2
1.4
$-t, (GeV/c)^2$
133081.2

Fig. 14

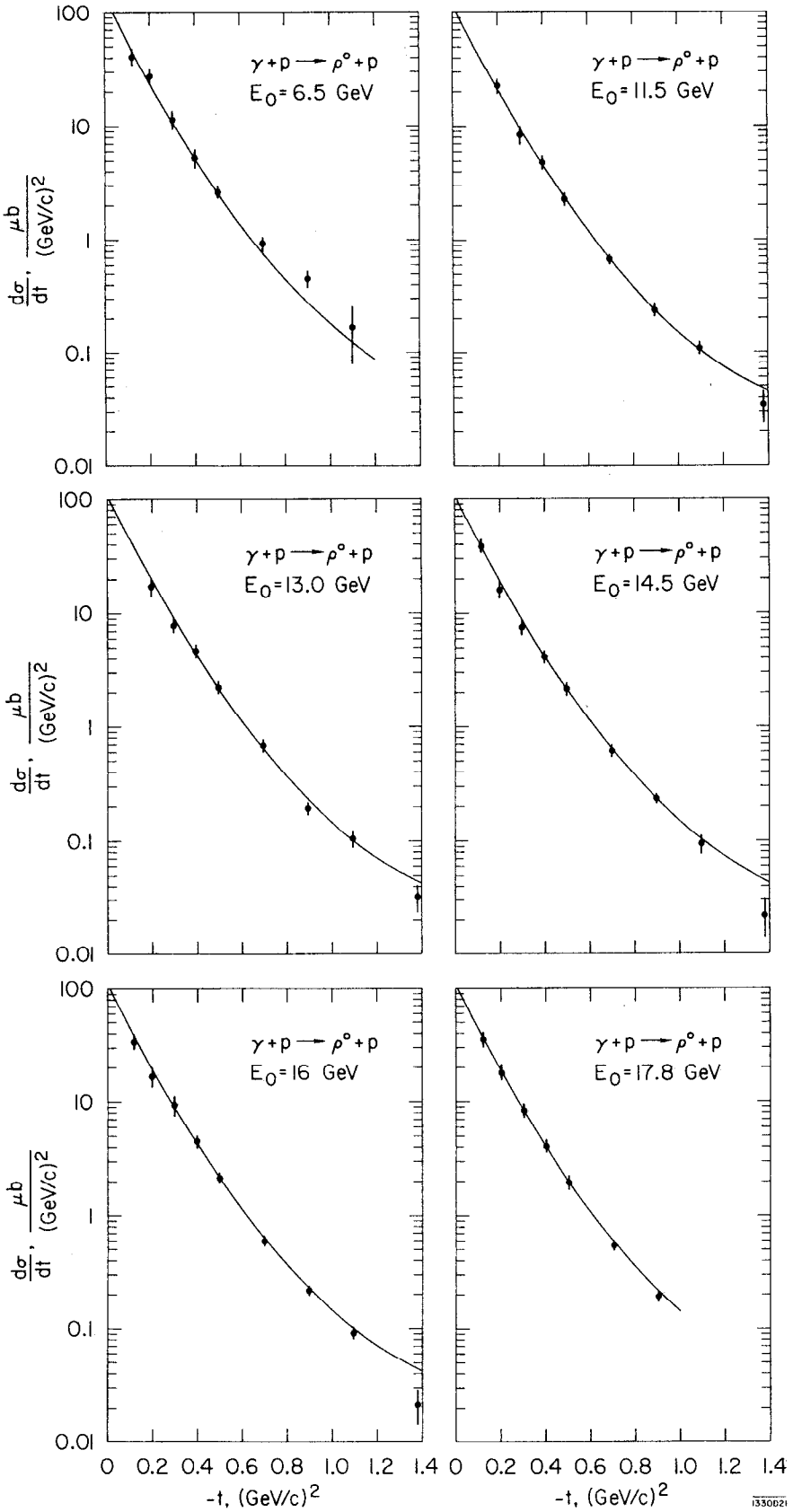
γ+p → ρ°+p
E0 = 6.5 GeV
γ+p → ρ°+p
E0 = 11.5 GeV
γ+p → ρ°+p
E0 = 13.0 GeV
γ+p → ρ°+p
E0 = 14.5 GeV
γ+p → ρ°+p
E0 = 16 GeV
γ+p → ρ°+p
E0 = 17.8 GeV
dσ/dt, μb/(GeV/c)²
100
10
1
0.1
0.01
0 0.2 0.4 0.6 0.8 1.0 1.2 1.4
-t, (GeV/c)²
1330021

Fig. 15

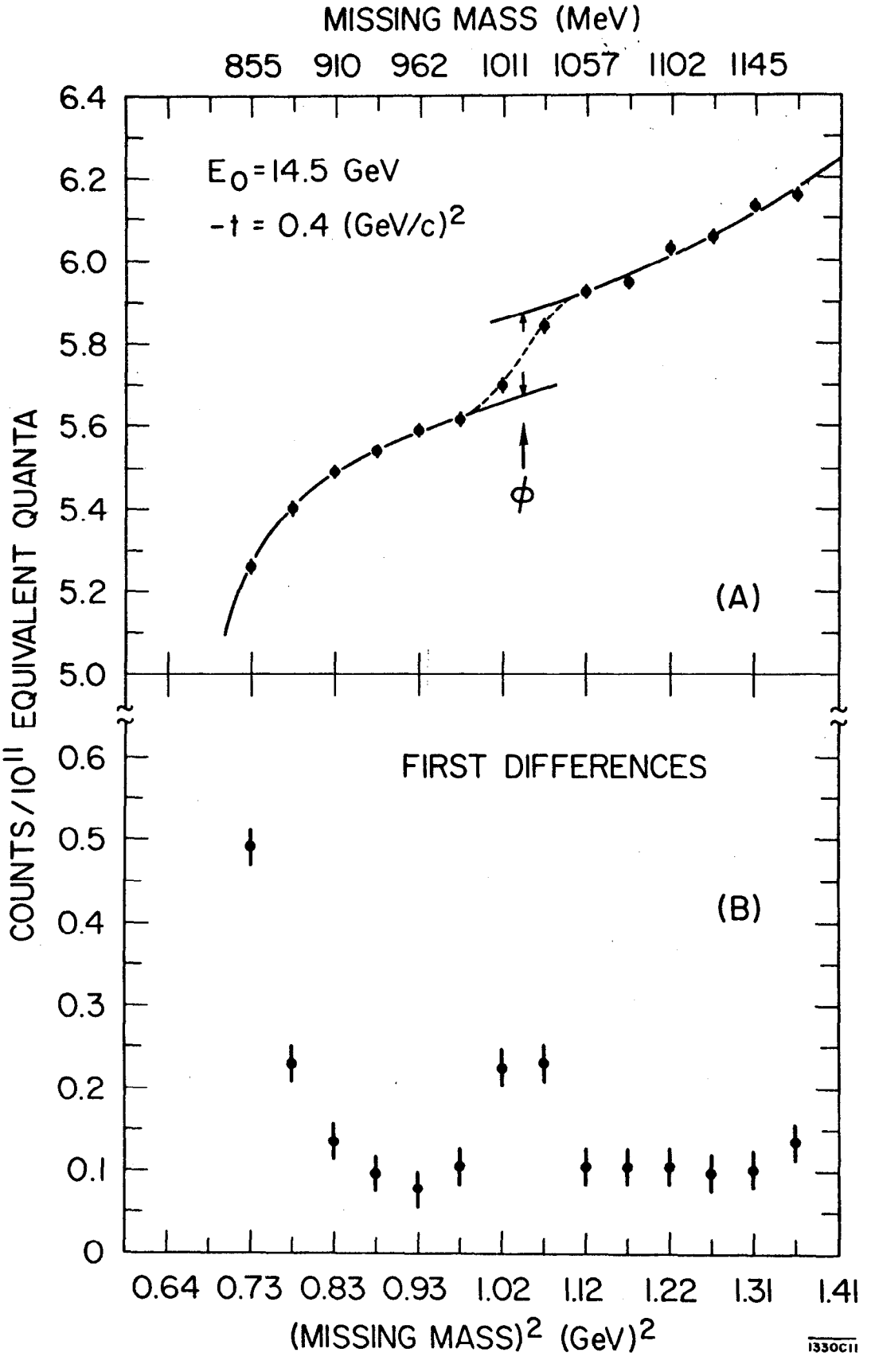
MISSING MASS (MeV)
855 910 962 1011 1057 1102 1145
E_0=14.5 GeV
$-t$ = 0.4 (GeV/c)^2
ϕ
(A)
FIRST DIFFERENCES
(B)
COUNTS/10^{11} EQUIVALENT QUANTA
6.4
6.2
6.0
5.8
5.6
5.4
5.2
5.0
0.6
0.5
0.4
0.3
0.2
0.1
0
0.64 0.73 0.83 0.93 1.02 1.12 1.22 1.31 1.41
(MISSING MASS)^2 (GeV)^2
1330C11

Fig. 16

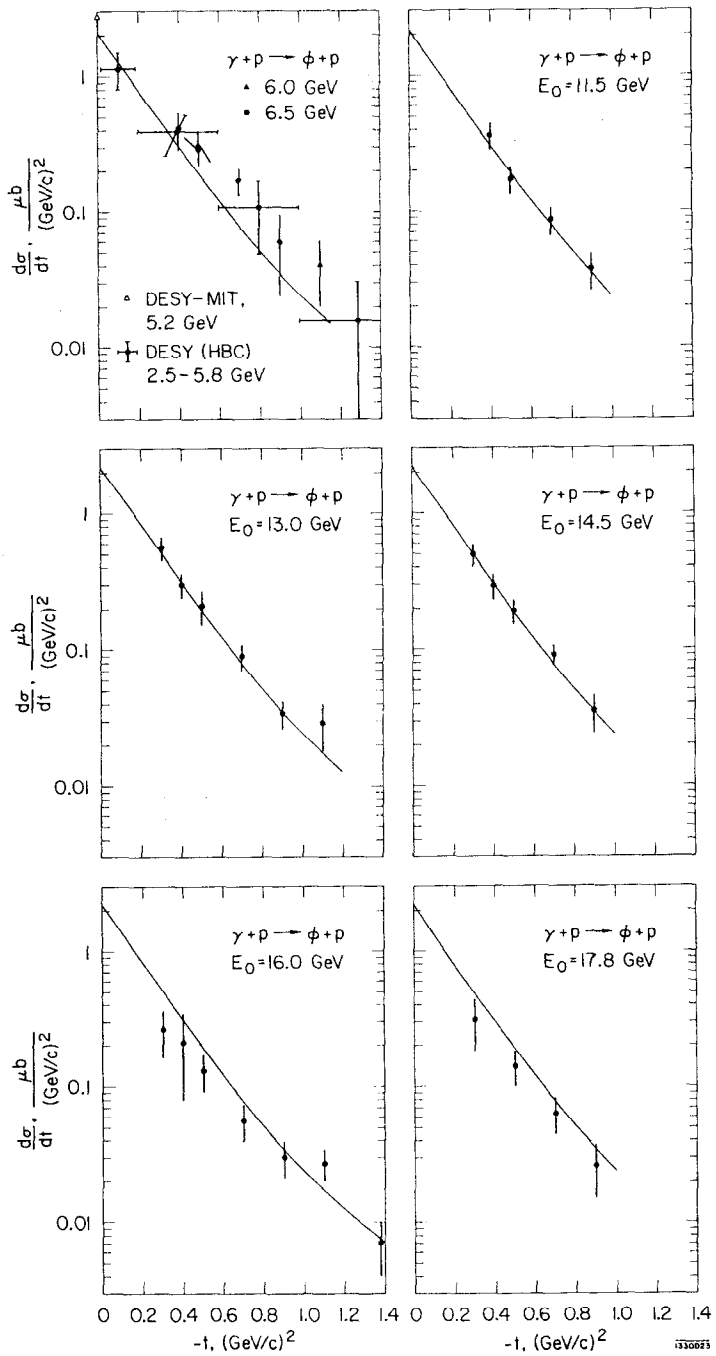
γ+p → φ+p
▲ 6.0 GeV
• 6.5 GeV
○ DESY-MIT, 5.2 GeV
DESY (HBC) 2.5-5.8 GeV
γ+p → φ+p E0=11.5 GeV
γ+p → φ+p E0=13.0 GeV
γ+p → φ+p E0=14.5 GeV
γ+p → φ+p E0=16.0 GeV
γ+p → φ+p E0=17.8 GeV
dσ/dt, μb/(GeV/c)²
1
0.1
0.01
0 0.2 0.4 0.6 0.8 1.0 1.2 1.4
-t, (GeV/c)²
133002-5

Fig. 17

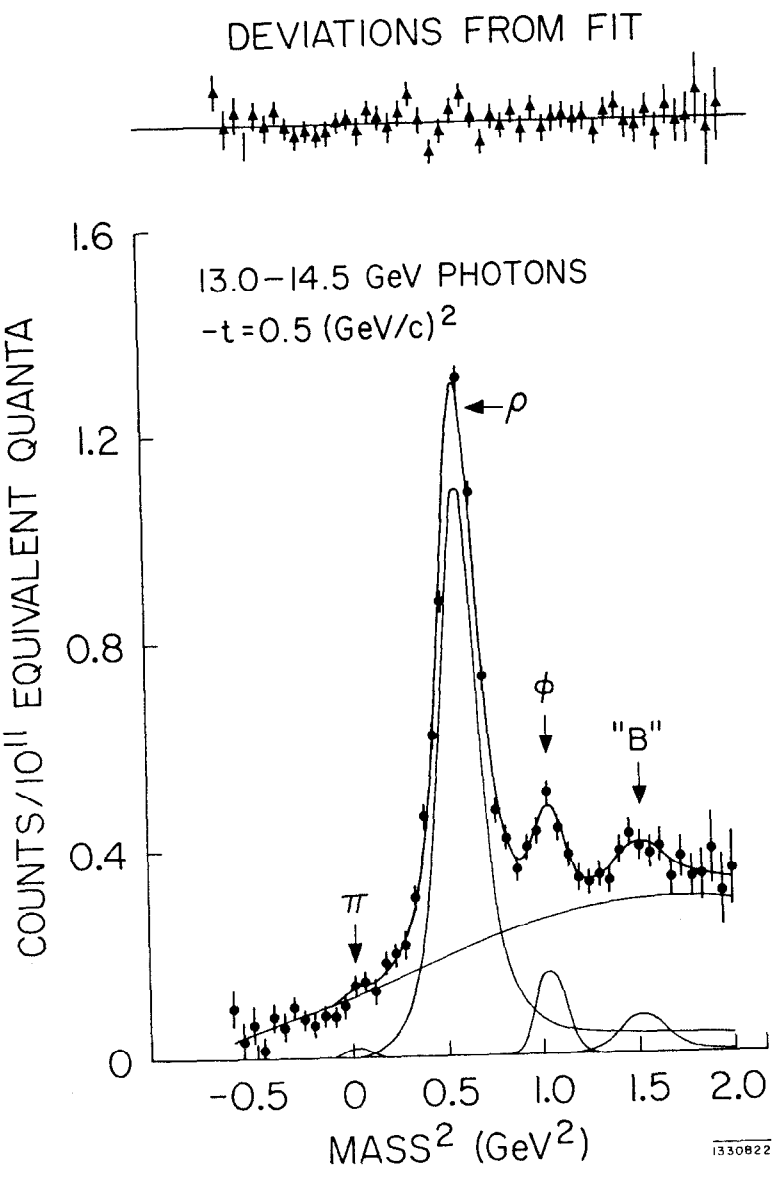
DEVIATIONS FROM FIT
13.0–14.5 GeV PHOTONS
-t=0.5 (GeV/c)^2
ρ
φ
"B"
π
COUNTS/10^{11} EQUIVALENT QUANTA
1.6
1.2
0.8
0.4
0
-0.5
0
0.5
1.0
1.5
2.0
MASS^2 (GeV^2)
1330822

Fig. 18

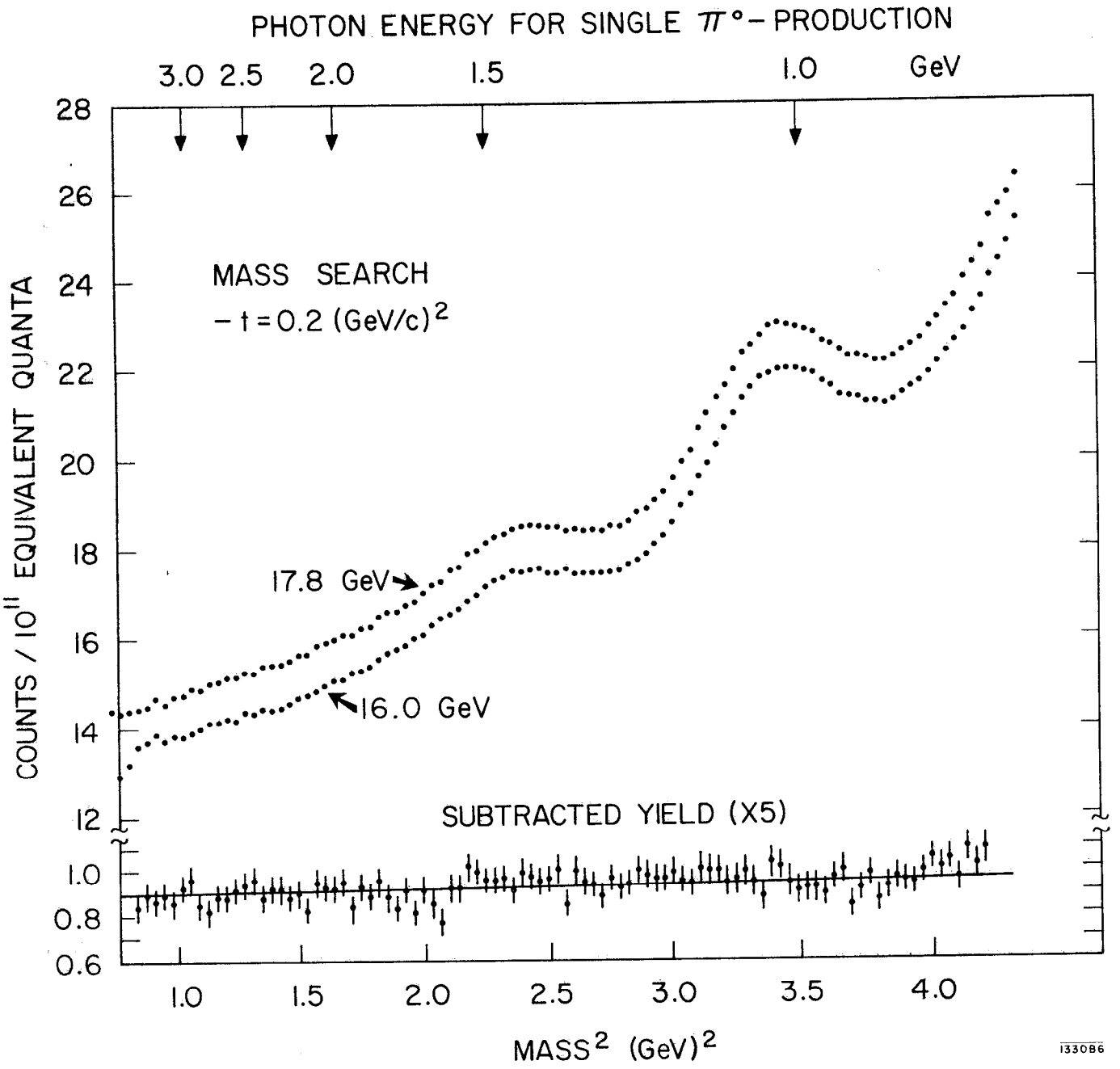
PHOTON ENERGY FOR SINGLE π°-PRODUCTION
3.0 2.5 2.0 1.5 1.0 GeV
MASS SEARCH
-t=0.2 (GeV/c)²
17.8 GeV
16.0 GeV
SUBTRACTED YIELD (X5)
COUNTS / 10¹¹ EQUIVALENT QUANTA
MASS² (GeV)²
133086

Fig. 19